THERMAL LENS MITIGATION AND MODELING OF CHROMIUM-DOPED ZINC SELENIDE LASER SOURCES

Thesis

Submitted to

The School of Engineering of the

UNIVERSITY OF DAYTON

In Partial Fulfillment of the Requirement for the Degree

Master of Science in Electro-Optics

by

Patrick A. Berry

UNIVERSITY OF DAYTON

Dayton, Ohio

May 2005

Thermal Lens Mitigation and Modeling of Chromium-Doped Zinc Selenide Laser Sources

APPROVED BY:

Peter E. Powers, PhD.
Professor,
Electro-Optics Program
University of Dayton
Committee Chairman

Kenneth L. Schepler, PhD.
Principal Scientist
Sensors Directorate
Air Force Research Lab
Committee Member

Joseph W. Haus, PhD.
Director and Professor,
Electro-Optics Program
University of Dayton
Committee Member

Donald L. Moon, Ph.D.
Associate Dean
Graduate Engineering Programs
& Research
School of Engineering

Joseph E. Saliba, Ph.D., P.E.
Dean
School of Engineering

Abstract

THERMAL LENS MITIGATION AND MODELING IN CHROMIUM-DOPED ZINC SELENIDE LASER SOURCES

Patrick A. Berry
University of Dayton

Advisor: Dr. Peter E. Powers

Cutting edge military and scientific applications require laser sources in the 2-5 μm region. These sources need to be compact and solid-state as well as tunable over a range of wavelengths. Divalent chromium-doped zinc selenide sources show great promise in this area due to their favorable properties such as room temperature operation, broad tunability between 2 and 3 μm as well as broad absorption bands allowing them to be diode pumped if necessary.

The development of chromium lasers has been hampered, however, by their susceptibility to thermal lensing. II-VI host materials tend to have high values for differential change in refractive index with temperature which, upon heating via a pump beam, results in a refractive index gradient. This thermal lens has a negative impact on the cavity stability and can result in laser sample destruction. The significance of thermal issues highlights the need for effective modeling techniques which can quantitatively predict lensing effects, increasing the efficiency and effectiveness of design and experimentation.

Modifying the physical specifications of a laser system such as cavity design and pumping style as well as changing the temperature management scheme can yield high returns in terms of reducing thermal issues. In order to reduce the experimental cost of investigating these improved thermal lensing mitigation techniques, it is vitally important to develop accurate and predictive models which will identify likely candidates for success. Mathematical models of proposed thermal lensing solutions were produced using finite element analysis software and used to determine the best design for experimental verification.

After material procurement and characterization, the chosen design was constructed for testing. The pass-through pumped thin disk laser with dual windows was simple to construct and showed no thermal issues for pulsed operation at suitable frequencies. By changing experimental parameters, this laser was made to demonstrate thermal issues at higher pulse repetition frequencies and lower outcoupler reflectivies. This type of laser was shown to be a good alternative to both the simple rod laser and the basic face-cooled thin disk laser.

Acknowledgements

I would like to thank Dr. Ken Schepler from the EO Countermeasures Technology branch of the Sensors Directorate at the Air Force Research Lab for his invaluable advice, answers, questions and overall guidance on this project. I would also like to thank my advisor Dr. Peter Powers from the University of Dayton for his help in both research and academic matters. Most importantly, I would like to thank my wife Leah for packing up and moving across the country to allow me to pursue my dreams; without you, none of this would have been possible.

Table of Contents

List of Illustrations

List of Tables

Chapter 1
Introduction

1.1 Background

The mid-IR wavelength region is important for a number of military uses such as remote chemical sensing, infrared countermeasures (IRCM), and target recognition and designation. In addition to military applications, scientific applications such as spectroscopy, environmental sensing, medicine and some manufacturing applications also require mid-IR sources. These applications, along with a lack of suitable existing sources, are driving a pressing need for robust, compact solid-state tunable mid-IR laser sources in the 2 to 4 μm wavelength range.

Laser sources consisting of chromium doped into II-VI host materials have the potential to fill many of these requirements. II-VI compounds, consisting of a group II transition metal and a group VI chalcogenide, have excellent IR transmission characteristics as well as low phonon vibration frequencies which reduce non-radiative transition rates even at room temperatures. In addition, when substituting for a Group II metal, chromium assumes a divalent ionization state which gives it a desirable energy level scheme. These features make II-VI compounds an ideal host. Divalent chromium has absorption in the 1.5 to 3 μm

range along with a laser transition in the 2.5 to 3 μm range. Chromium II-VI lasers have been demonstrated using a number of host materials such as zinc selenide, cadmium manganese telluride and cadmium selenide.[1, 2, 3]

1.2 Problem Statement

The development and widespread use of chromium lasers has long been hampered by the problem of thermal lensing. Thermal lensing occurs when variations in the refractive index across the material, arising from thermal gradients, alter the phase profile of light passing through the material, effectively acting as a lens. This can cause cavity instability as well as material damage from focusing at high powers. The thermal gradients that cause thermal lensing typically come from excess heat generated by pumping, either through the quantum defect or from non-radiative losses.

Table 1: Thermomechanical properties of various laser hosts

Material	κ (W/mK)	dn/dT (10^{-6}/K)
ZnS	17	46
ZnSe	18	70
YAG ($Y_3Al_5O_{12}$)	10	8.9
YLF ($YLiF_4$)	5.8	-2.0, -4.3
LG-750 (phosphate glass)	0.6	-5.1
Sapphire (Al_2O_3)	28	12

The degree to which a material exhibits thermal lensing is dictated by its differential index change with temperature (dn/dT) along with the thermal

conductivity. As seen in Table 1, II-VI hosts tend to have higher values for both of these properties than other hosts such as Yttrium-Aluminum-Garnet (YAG) or Yttrium Lithium Fluoride (YLF), making thermal issues with these types of lasers an important problem.[4] A number of designs for thermal lens mitigation resonators are found in the literature and include the fiber waveguide-based laser, ziz-zag mode slab laser and the thin disk laser. While some progress has been made in addressing this problem using thin disk laser designs, there is still room for improvement.[5]

1.3 Research Objective

The objective of this research was to characterize thermal effects in chalcogenide lasers through modeling and to develop and investigate improvements on existing thermal lensing mitigation methods. The goal of the modeling portion of the research was to become familiar with the likely physical manifestations of thermal issues as well as the effects of changing various design parameters. The results of the modeling were to allow an informed choice of laser designs in order to reduce overall experimentation time and cost by eliminating designs unlikely to produce desired results. The goal of the experimental portion of the research was to quantify losses and verify the viability of a chosen design.

1.4 Methodology

Designs for thermal lensing mitigation methods were modeled using a commercially available finite element analysis package, FemLab®. This package

has a built-in CAD interface to produce model geometries. All pertinent material parameters were entered into this program and solutions for steady state heat distribution were produced. This data was then processed using MatLab® (outlined in section 4.3 Model Results) to produce the calculated thermal lens power and the average temperature rise of each design. These criteria, along with practical considerations (discussed in Chapter 2 Proposed Laser Designs) were used to select a design that would be optimal for experimental work. Once a likely design candidate was established, it was constructed and put through a series of experiments design to gauge its suitability for different types of operation.

Chapter 2
Proposed Laser Designs

2.1 Laser Design Variations

The construction of a high power laser with low thermal lensing requires a studied consideration of laser geometry. Several methods for mitigating thermal gradient issues in laser resonators can be found in the literature. These include the fiber waveguide-based laser, the zig-zag mode slab laser and the thin disk laser. All three types of designs were considered for study in this research.

A laser using a fiber waveguide as a resonator would have to contend with the increasing intrinsic absorption loss and material dispersion of the fiber as the wavelength passes 1.55 μm. Fiber technologies which can alleviate or mitigate these losses are limited at this time to either hollow waveguides or chalcogenide glasses. Hollow waveguides made from plastic, glass or crystal tubes typically have highly reflective dielectric coatings on the interior surface.[6] These types of fibers were not likely to be useful as fiber laser gain media unless they could be filled with dopant-containing materials and still retain their properties. Chalcogenide glass fibers were another possible candidate for high power mid-IR fiber lasers, but at the time of this research, none had been produced which had

the required material properties as well as the required active ions.[7] The current state of the art in mid-IR fibers eliminated this type of laser as a possibility.

A zig-zag mode slab laser is one which is edge pumped and has a resonator mode which bounces back and forth between the cooled top and bottom faces. The path of this mode could average out the effects of thermal gradients but this design also requires higher pump powers due to poor coupling efficiency. As much as 75 W could be needed for a 1mm by 3 mm slab.[8] Since the current max pump power available at this wavelength was 40 W, this design was not feasible.

This research focuses on the development of mitigation methods based on thin disk geometries. The thin disk concept, originally proposed as an alternative to the traditional solid rod design, has a high diameter to thickness ratio and is intended to be cooled on one or both faces.[9] By increasing the cooling surface for a given volume of laser material, heat dissipation is increased and overall material temperature is decreased.

One of the drawbacks of the thin disk is that the thin disk has a shorter distance in which the pump energy can be absorbed by the active ions. While it is possible to increase the doping level to get more absorption per pass, there is a limit to the amount of chromium which can be present before nonradiative relaxation occurs. The lifetime and threshold are both directly affected by nonradiative relaxation and thus by the doping level. The practical requirement that this imposes is that multiple pump passes are usually necessary for sufficient energy to be absorbed.

2.2 *Face Cooled Thin Disk*

The most basic thin disk design considered in this research, and indeed the baseline by which other designs were measured, is the face cooled thin disk. In the face cooled thin disk, the material geometry has a high diameter to thickness ratio as well as a rear face that is HR coated at both the pump and laser wavelengths. This type of laser has demonstrated benefits in terms of thermal issue management and has been shown to be viable at extremely high powers. [10, 11]

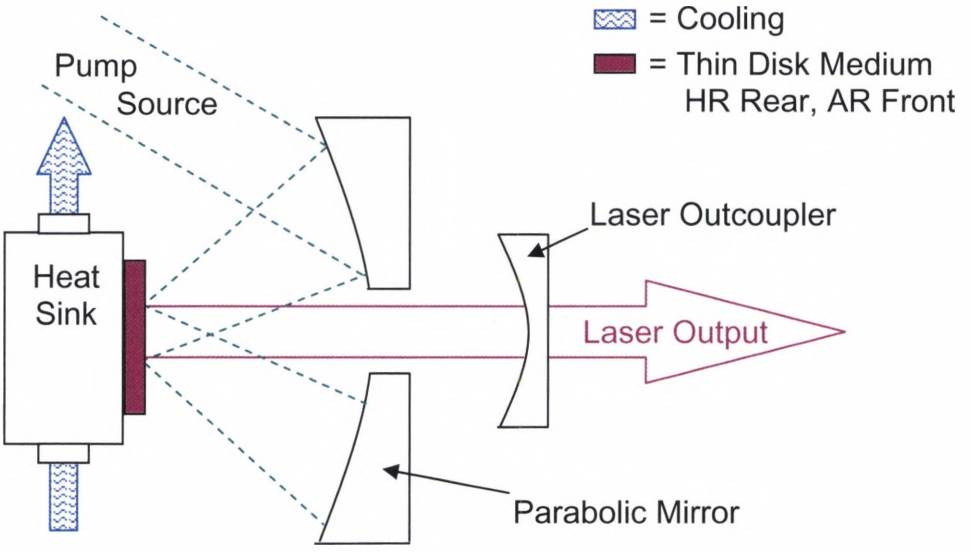

Figure 1: Face cooled thin disk design

A typical laser setup for the basic face cooled thin disk can be seen in Figure 1. The laser medium is typically AR coated on its front face and HR coated on its rear face, with both coatings optimized for both the pump and laser wavelengths. The rear face thus acts as a cavity mirror and also allows for attachment to a heat sink using some type of bonding method such as soldering

or epoxying. Due to the short absorption path, the pump beam is typically imaged multiple times on the laser material using a parabolic mirror or even more complicated reflection schemes in order to achieve up to sixteen passes.[12]

The strong benefits of this design are that it allows cooling across the entire rear face of the laser material to alleviate thermal gradients and the rear reflective design automatically doubles the pump path length. The shortcomings of this particular design are that the laser material must be subjected to what can be a time consuming and costly HR and AR coating process. It also must then be subjected to a bonding process, either soldering or epoxying of the rear face to the heat sink. This not only runs a high risk of damaging the laser material, it also permanently mounts the laser material to that heatsink. A more flexible and lower risk mounting system would be highly beneficial.

2.3 *Ring and Face Cooled Thin Disk*

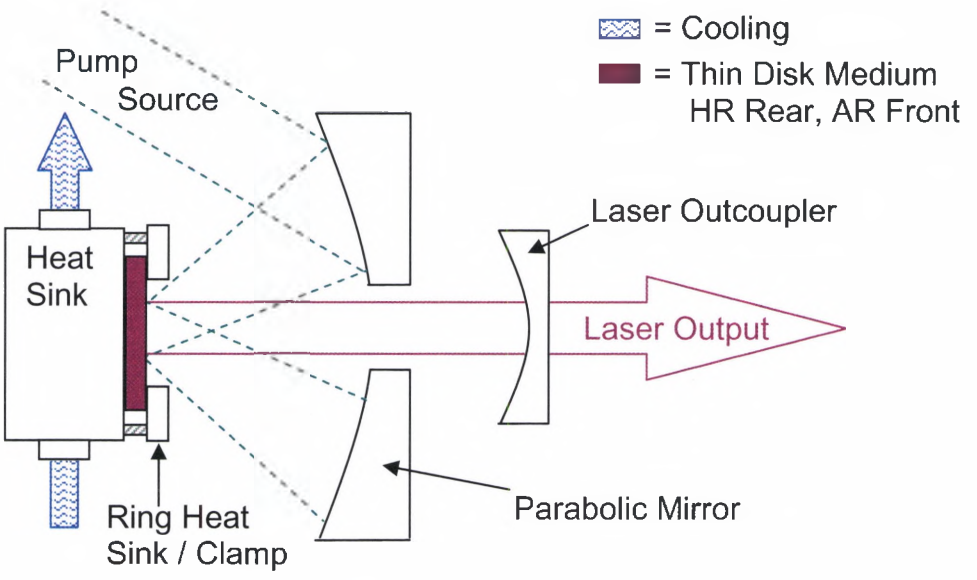

Figure 2: Ring and face cooled thin disk design

To eliminate the mounting of the laser sample to a heat sink, a clamp could be used to hold the laser sample tightly to the heatsink. This clamp would generally take the form of a solid piece of heat sink material with a hole in the middle to allow passage of the pump beam, forming a ring around the front face of the laser sample. As seen in Figure 2, this design incorporates easy mounting while still retaining the benefits of the face cooled design. The clamp, because it is screwed directly into the rear heat sink, would help to remove heat from the front face, acting as an additional heat sink along the outside of the front face of the laser sample. The drawback of this design is that it still requires AR coating on the front face and HR coating to the rear face of the laser sample, again, a costly and possibly time consuming and damaging process.

2.4 *Ring and Face Cooled Thin Disk with Window*

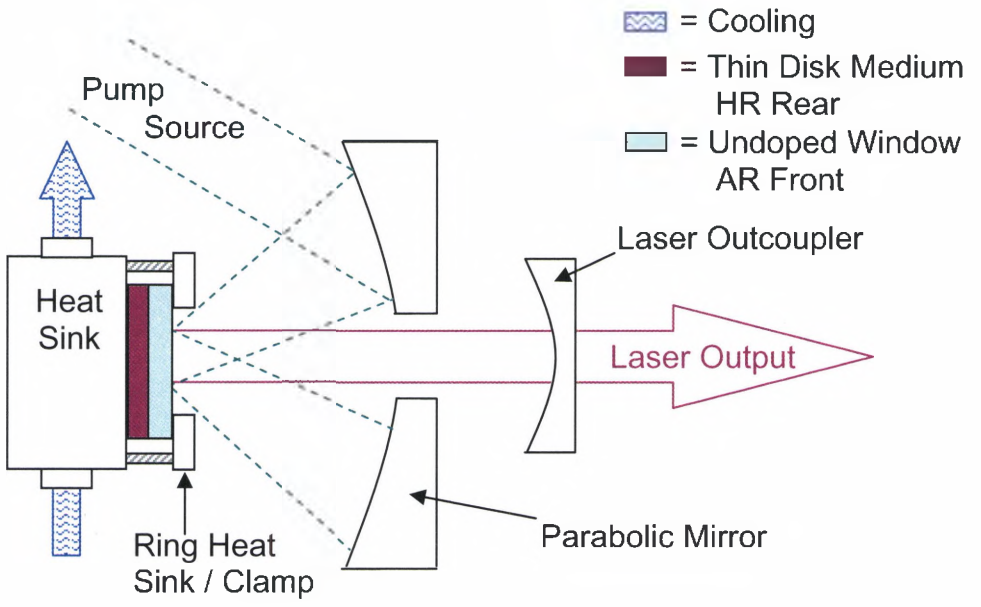

Figure 3: Ring and face cooled thin disk with window design

While cooling across the back face of the laser material has been addressed in the previous designs, it is desirable to cool the front face of the sample as well. This could be achieved by adding an undoped 'window' to the front face of the laser sample, as seen in Figure 3. This window would have the additional benefit that it could be AR coated, eliminating one of the needed coatings to the laser sample. This window also would bear the brunt of possible damage from the clamping process instead of the laser sample. The drawback to this design would be that the laser sample still needs to be coated HR on its rear face and there could be significant losses at the interface between the laser sample and the window if the surfaces are not perfectly matched.

2.5 Pass-Through Pumped Thin Disk

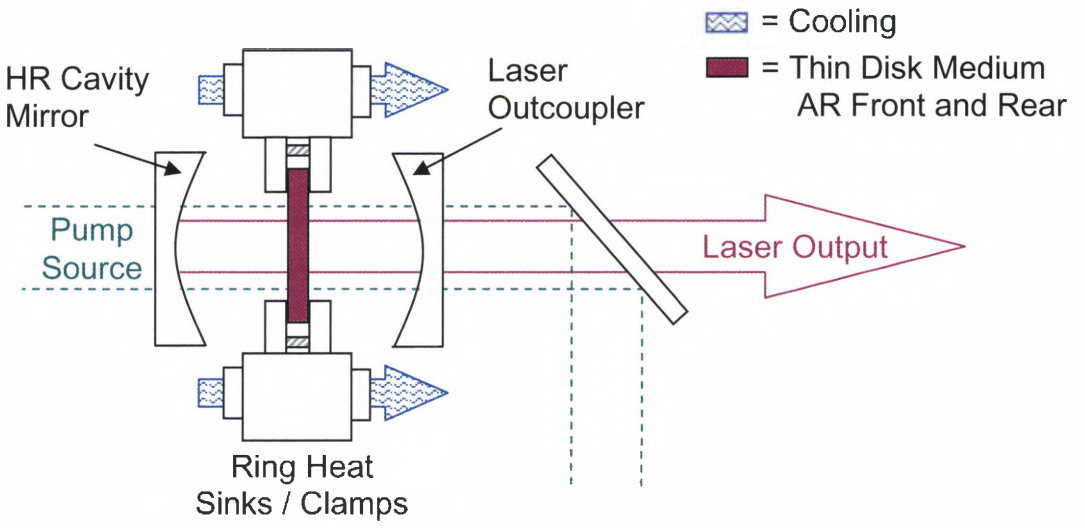

Figure 4: Pass-through pumped thin disk design

To eliminate the need for the HR coating on the back of the laser sample, a pass-through geometry can be used. The basic pass through design, seen in Figure 4, would be a thin disk held between two pieces of heat sink material with holes to allow the pump beam to pass through. This design has half the number of effective pump passes as the rear-reflective face cooled designs, but it is also much easier to construct than complicated multi-pass setups. This configuration also suffers from the need to have both sides AR coating to avoid suffering Fresnel losses and it eliminates the rear face cooling, but it is also the simplest of all the designs. This design would be likely to have the highest thermal gradients and would be most likely only be useful for initial testing of samples without any preparation.

2.6 *Pass-Through Pumped Thin Disk with Dual Windows*

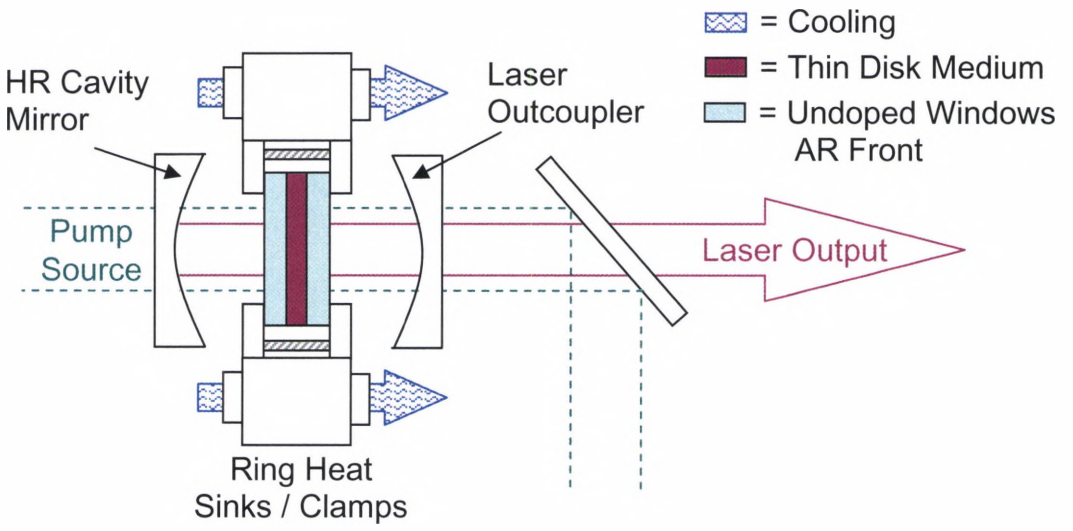

Figure 5: Pass-through pumped thin disk with dual windows design

Combining the previous designs produced a design in which the uncoated laser sample is sandwiched between two index-matched, undoped windows which would serve to cool the front and rear faces while allowing the pump beam to pass through. These windows, seen in Figure 5, could be AR coated on their outside faces. While this may seem to be no advantage over AR coating the laser sample, the benefit is that undoped windows are inexpensive relative to laser samples and sets of windows can be coated in a single coating run and then used with any number of laser samples, provided that they have the same index of refraction. This also eliminates the risk to the laser samples of breakage during coating or shipping.

As in the previous design, the pump beam only passes through the laser medium once and is dumped out using a beam splitting mirror at 45° which limits

the efficiency of the laser. The efficiency of this design could be improved by implementing a multi-pass pumping scheme. A simple way to do this would be to use a mirror normal to the beam path to reflect the pump beam back through the cavity instead of dumping it. Other multi-pass schemes could be used as well.

2.7 Design Conclusions

There are a number of possible designs that could work well for this research. It would not be feasible to finalize the design, construct and test every one of these designs. It was concluded that, in order to maximize experimental resources, models of each design should be created and simulations run to determine which model was most likely to succeed in filling the research requirements. The successful design should be efficient, low cost and easy to construct while still limiting thermal lensing and overall temperature rise in the laser medium.

Chapter 3
Material Characterization

3.1 Material Property Considerations

Before proceeding with the modeling, the material properties of the laser materials had to be characterized. The accuracy of the modeling process depended heavily on the accuracy of the material properties used to run the simulations while the success of the experimental stage depended on the qualities of the laser samples. Laser samples of chromium zinc selenide would have to be procured that adhered to certain specifications.

In a laser medium, it is important to have an active ion concentration that is high enough to enable high pump absorption as well as to prevent bleaching. In general, the shorter the pump absorption path, the higher the ion concentration should be. However, in chromium zinc selenide, it has been shown that high chromium concentrations lead to reduced excited state lifetimes, most likely arising from increased nonradiative relaxation.[13] This lead to a situation where, due to the thin disk geometry, high absorption as well as long fluorescence lifetimes were both desired, but were to some extent, mutually exclusive. The samples would have to have a long enough fluorescence lifetime that

nonradiative relaxations would not be an issue but also have high enough doping so that maximum pump power would be absorbed.

Two samples of chromium zinc selenide were obtained through a long term loan from Coherent Technologies, Incorporated. These samples, assigned the designations CR44 and CR45, were 8 mm diameter disks which were around 2 mm thick and were originally created by Shayda Technologies in Chicago, IL. Four additional samples, to be designated CR46 through CR49, were commissioned from Shayda for use in this research project. Shayda uses a diffusion doping process to make the chromium zinc selenide which limits the accuracy with which they can dope a given sample. Due to this, test samples of chromium zinc selenide with different doping levels were analyzed to zero in on the optimal diffusion process time. Once four were found with the desired characteristics, they were accepted into the inventory. These samples were also 8 mm thick and around 2 mm thick.

The analysis of the test samples showed that the fluorescence lifetimes tended to decrease as the absorption (and thus dopant level) increased. These four samples were specified to have fluorescence lifetimes longer than 1 μs while still having significant absorption at the pump wavelength. At lifetimes below 1 μs, non-radiative transitions would likely become a large negative factor. The absorption levels did not need to be quantified beyond a general high / medium / low rating.

3.2 *Fluorescence Lifetime of Laser Samples*

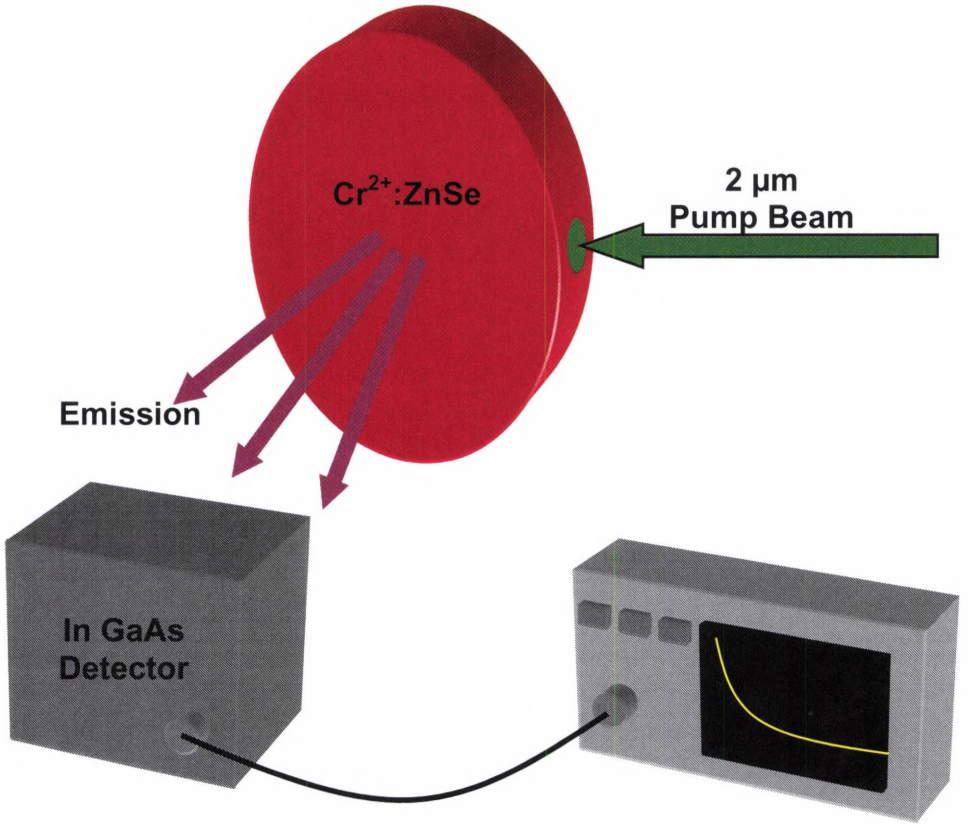

Figure 6: Fluorescence lifetime measurement

A fluorescence emission with a lifetime of τ will have an exponential decay that varies with time as in (1). If the natural log of this data is plotted versus time,

$$\exp\left[-\frac{t}{\tau}\right] \tag{1}$$

the slope of the resulting line should be the reciprocal of the lifetime τ. If τ was a distribution of lifetime values, then the slope of a linear best fit line would represent an average value for τ.

Fluorescence lifetimes of the laser samples were measured using a set up as shown in Figure 6. A Swartz-Electro-Optics holmium laser operating at 2 µm, with a PRF of 1 Hz and pulse widths on the order of 100 ns was used to side

pump the laser samples. A modified InGaAs detector, fitted with a long-pass 2.07 μm filter, was connected to an oscilloscope to collect the emitted pulse shapes. This information was then processed using MatLab® (detailed code can be seen in Appendix Two: MatLab Code: Listing 1: ExponetialFit.m) to produce a semi-log plot of the decay along with the calculated fluorescence lifetime.

An example of this measurement from sample CR44 can be seen in Figure 7. This figure shows that the natural log of the decay is not a perfectly straight line. The higher slope at the beginning of the graph could come from some pump signal passing through the filter. The data was not sampled until around 2 μs had passed, so it is not likely that the pump pulse played a large part in this higher slope region. More likely it arose from variations in the chromium concentration through the sample. Areas of higher concentration would have shorter lifetimes and steeper slopes. The lifetime data for all the samples can be seen in Table 2.

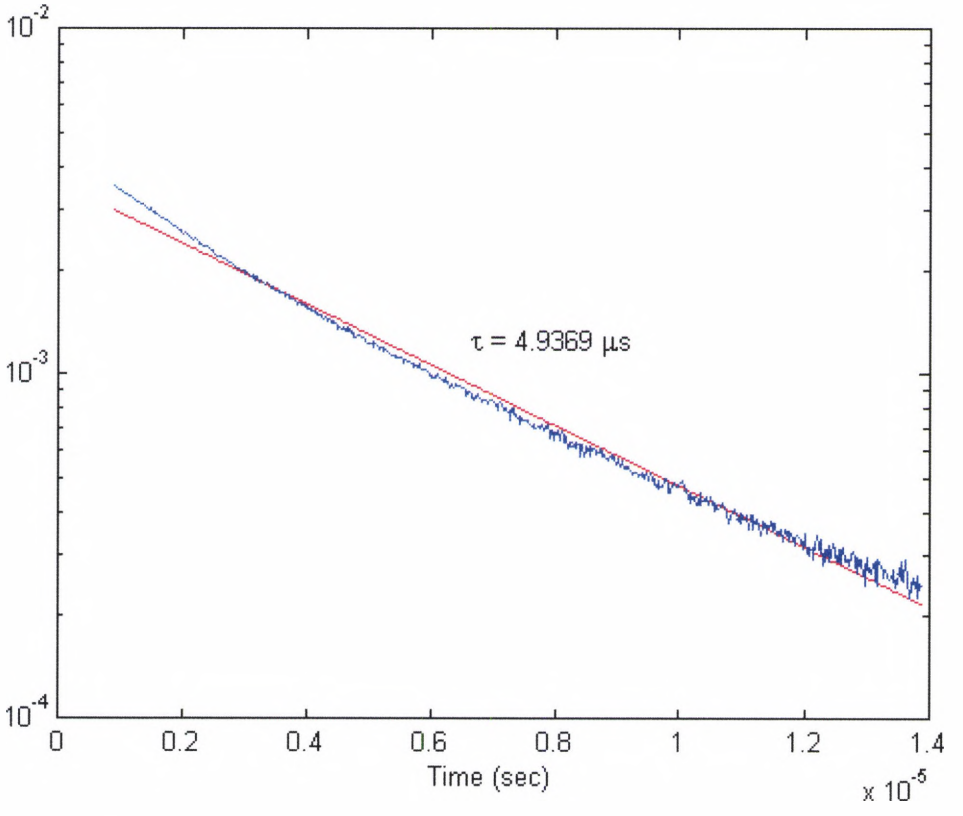

Figure 7: Fluorescence lifetime measurement of sample CR44

Table 2: Fluorescence lifetimes of chromium zinc selenide samples

Sample Designation	Lifetime (µs)	Absorbance	Thickness (mm)
CR44	4.77	Low	2.12
CR45	4.99	Low	1.78
CR46	3.13	High	2.27
CR47	2.86	High	2.25
CR48	2.24	High	1.88
CR49	3.86	Medium	2.27

3.3 *Absorption of Laser Samples*

The absorbance of the laser samples was measured with a Cary 5000 UV-Vis spectrophotometer. These samples were run from 500 to 2500 nm at 3 nm resolution. The absorbance data can be seen in Figure 8. In this figure, the three samples with the longest lifetimes show low to medium absorption in the 1500 to 2000 nm range while the three samples with low lifetimes show absorptions that are off the scale.

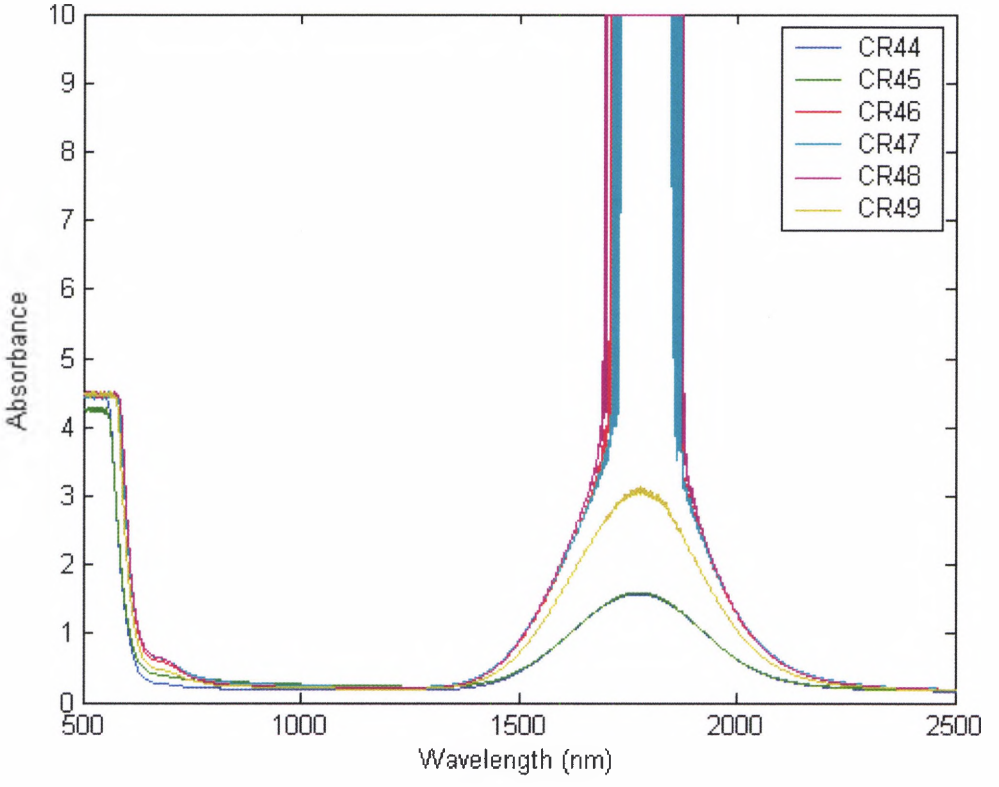

Figure 8: Laser sample absorbance data

Chapter 4
Thermal Lens Modeling

4.1 Modeling Approach, Assumptions and Limitations

One of the main goals of this research was to develop a modeling system that could be used to gain an understanding of thermal lensing as well as to help expedite the development of better laser designs. With this in mind, it was important to not only construct models of the proposed laser designs but to also study the effects of variations in the model parameters on the simulation results. These extra steps are needed to eliminate systematic errors inherent in the modeling assumptions from affecting the results and to establish a baseline model from which the proposed designs can be constructed.

To simplify the modeling process, certain assumptions were made. The laser source was assumed to be uniformly absorbed along the depth of the laser sample. This is not strictly true unless the thickness is small in comparison to the 1/e absorption depth. Multiple passes would tend to even out absorption at different sample depths, but since this model assumes a double pass, this assumption should be verified if the model accuracy is in doubt. Also, the heat sinks are assumed to be perfect heat sinks that maintain a constant temperature

on their surface. Lastly, conductive cooling by air is neglected such that all non-heat sink surfaces are considered to be insulating.

In order to allow the models to address differences in pump beam quality, the pump beam was assumed to have transverse pump beam profiles of either Gaussian (n = 1), super-Gaussian (n = 2) or top-hat, i.e. super-Gaussian (n = 25). These beams would be of the form in (2), where x_0 and y_0 define the center point of the beam, n is the order, and σ is the beam radius at which the value of the function drops to $1/e^2$. The shape of these profiles can be seen in seen in Figure 9.

$$f_n(x,y) = \exp\left[-\frac{2\left((x-x_0)^2+(y-y_0)^2\right)^n}{\left(\sigma^2\right)^n}\right] \tag{2}$$

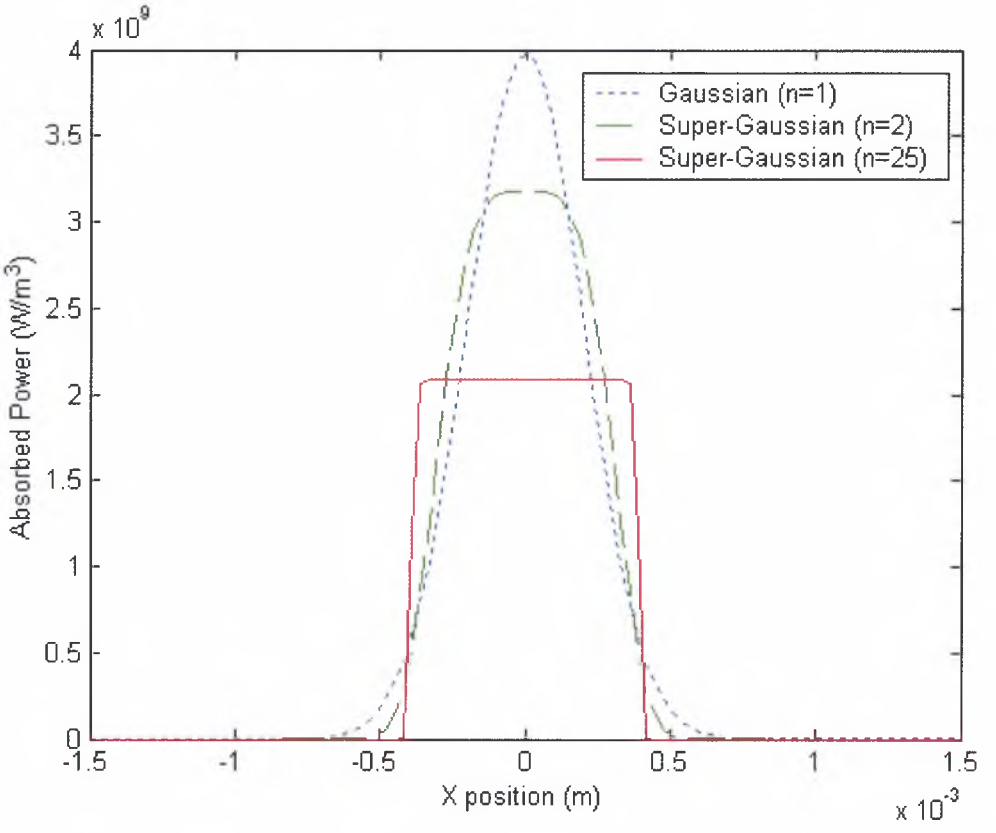

Figure 9: Transverse Beam Profiles

An integration factor for each of these profiles had to be calculated to normalize each one to 1 W of absorbed power. Custom MatLab functions (seen in Appendix Two: MatLab Code, Listing 3: HSIC.m and Listing 4: HSG.m) were used to calculate the heat source (Gaussian) and heat source integration constant for the three beam profiles. Two additional custom functions (seen in Appendix Two: MatLab Code, Listing 5: HSICR.m and Listing 6: HSGR.m) were used to verify that the integration constants were essentially the same for cylindrical co-ordinates. Using the results of these calculations, the integration constants were applied in the model as in (3)-(5), below, where σ is the pump beam radius (in mm) and Δz is the thickness of the geometry (in mm). These

constants would then be used as in (6) for the power absorbed at a given x, y position.

$$IC_1 = \frac{2}{\pi\sigma^2\Delta z} \tag{3}$$

$$IC_2 = 0.798\frac{2}{\pi\sigma^2\Delta z} \tag{4}$$

$$IC_{25} = 0.525\frac{2}{\pi\sigma^2\Delta z} \tag{5}$$

$$f_n(x,y) = IC_n * \exp\left[-\frac{2\left((x-x_0)^2+(y-y_0)^2\right)^n}{\left(\sigma^2\right)^n}\right] \tag{6}$$

One of the limitations of this modeling system is that it assumes a steady-state solution, so that the time evolution of the heat flow is not apparent. This type of information could be extremely useful in understanding the thermal behavior of these materials under different pumping schemes from pulsed to CW but was beyond the scope of this project.

4.2 Model Construction

The models were constructed using the newest version of FemLab® 3.0a, version number 3.0.0.228. The first step in the model construction process was to recreate the proposed model geometry using the program's CAD interface. In this step it is important to faithfully recreate the important elements of the design while minimizing the extraneous details. This step is important due to the fact that the complexity of the model and therefore the amount of time and memory required in solving the model are directly related to the size of the model and the number of surfaces. Along these lines, each model was pared down to just the

laser material, heat sinks and, when needed, undoped windows. The size of the heat sinks in the models could be minimized due to the third model assumption of perfect heat sinks. This meant that the only important part of the heat sink was the surface that was in direct contact with the laser material or window. To illustrate this, Figure 10 through Figure 14 show how each of the proposed designs were 'translated' into simple model geometries.

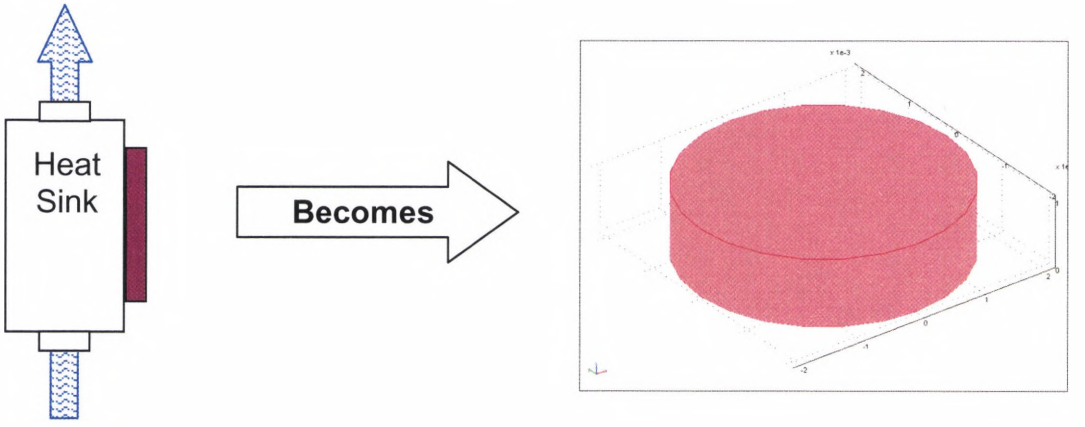

Figure 10: Basic face cooled design translation to model geometry

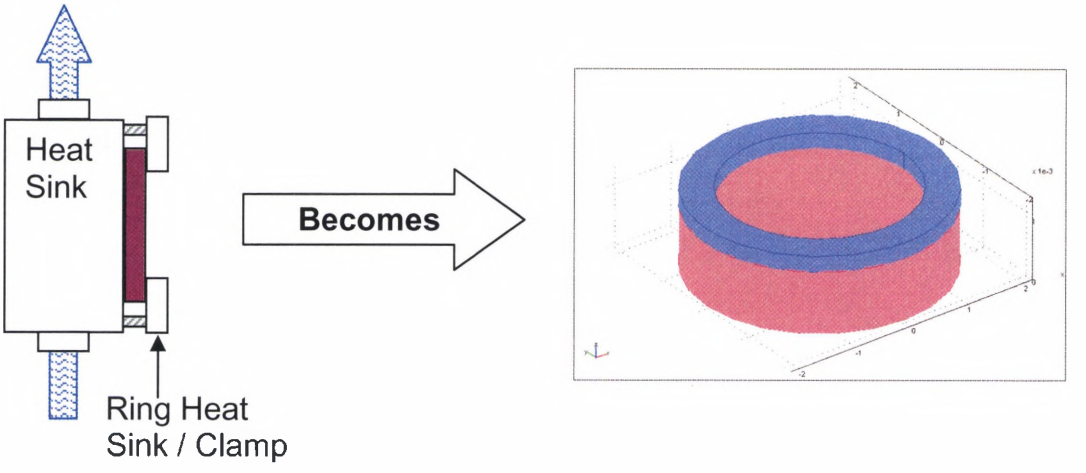

Figure 11: Ring and face cooled design translation to model geometry

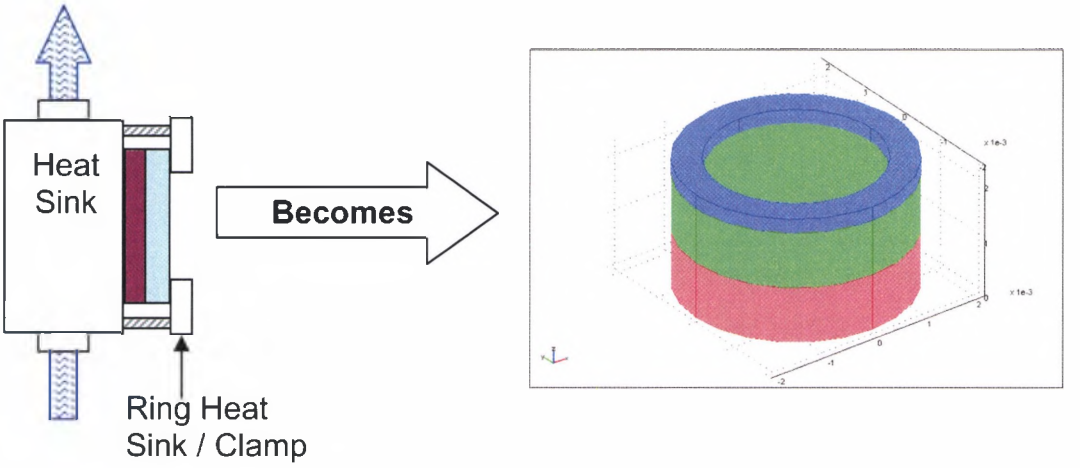

Figure 12: Ring and face cooled with window design translation to model geometry

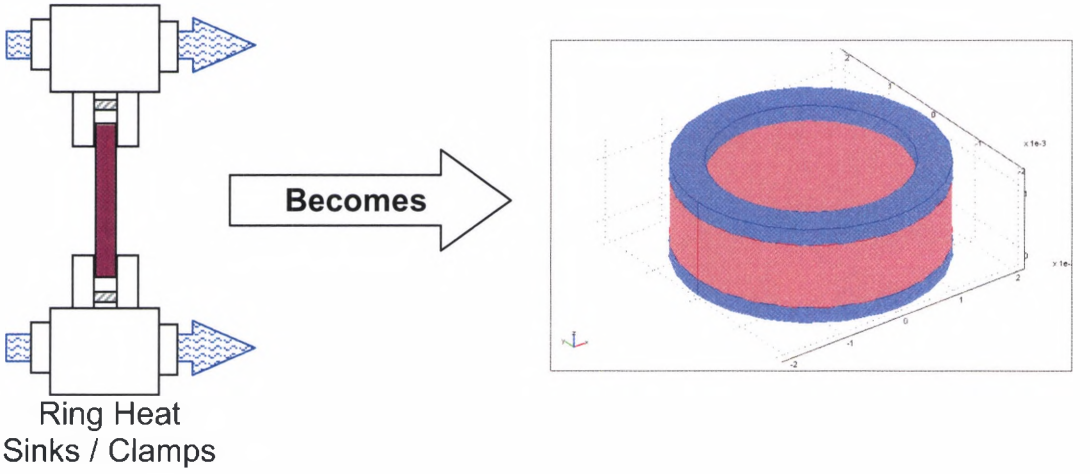

Figure 13: Pass-through pumped design translation to model geometry

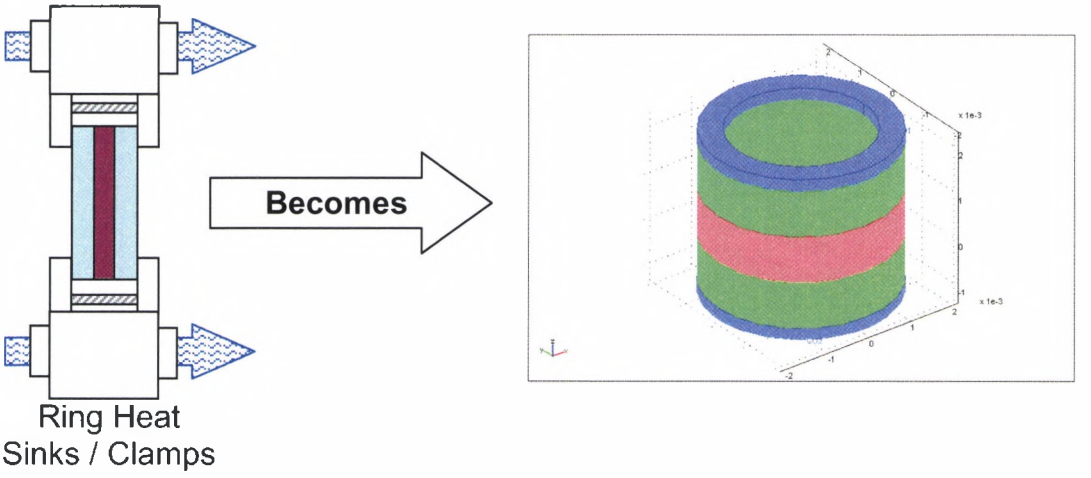

Figure 14: Pass-through pumped with dual windows design translation to model geometry

Once the model geometry was established, boundary conditions and subdomain material parameters were set according to the material properties of the system. For an in-depth discussion and example of model construction using FemLab® 3.0a, see Appendix One: Detailed Model Construction Process.

4.3 Model Results

FemLab® provided the solutions to the steady-state systems as data structures which contained all of the relevant temperature and geometry data. It also provided a visual display of the solution in its post-processing mode. These solutions showed the temperature distribution along a slice along one axis through the origin. As an example, the solution for the 4-mm basic face cooled thin disk design can be seen in Figure 15. This figure shows the high heat load in the center of the disk caused by the pump beam.

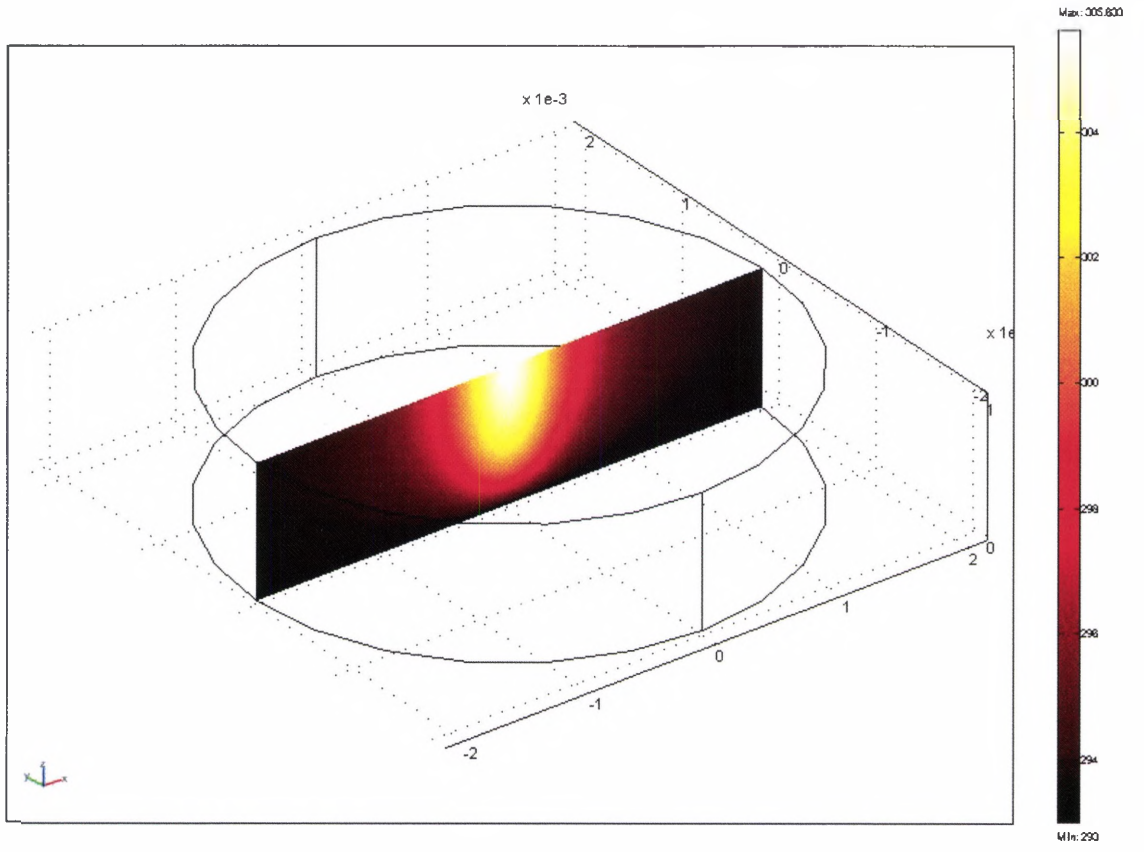

Figure 15: Simulation solution of 4 mm diameter, 1 mm thick face cooled thin disk pumped with a Gaussian (n = 1) beam with σ = 0.4 mm

Once the simulation had been run in FemLab®, the solved data structure was exported to MatLab and processed to determine the calculated thermal lensing power and the maximum average temperature rise. This process was started by integrating the temperature along the z-axis (the thin axis of the thin disk) which produced a two-dimensional temperature gradient surface. An example of the resulting gradient surface can be seen in Figure 16. This figure shows the average temperature rise (relative to the heat sink temperature) over the entire disk

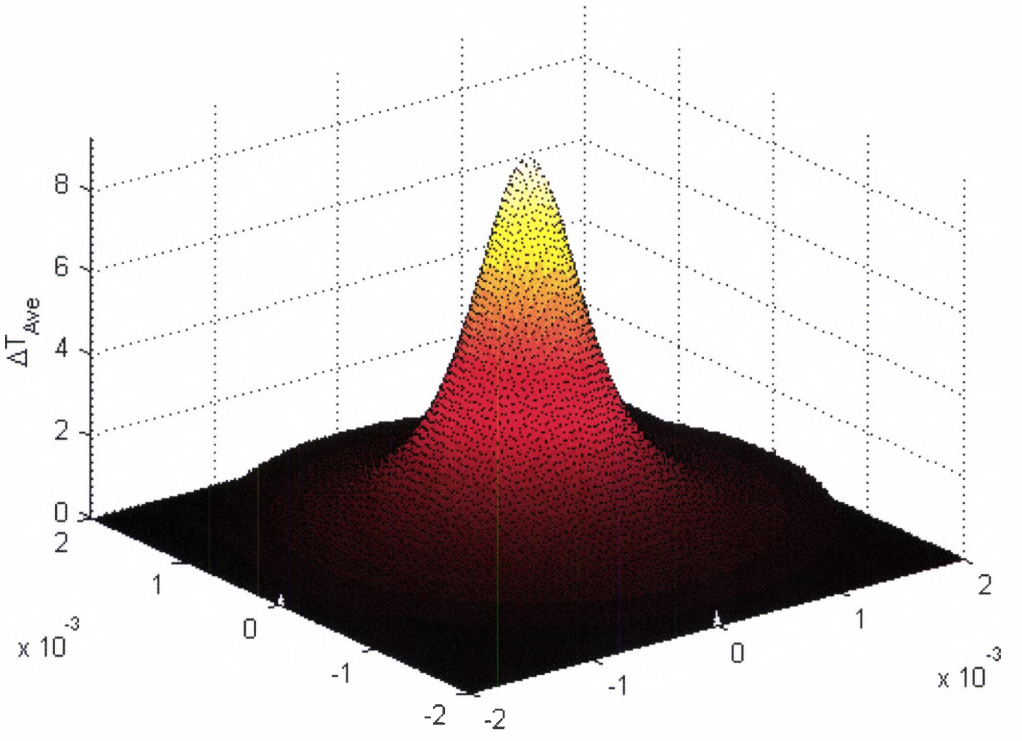

Figure 16: Temperature gradient surface for previous 4 mm face cooled thin disk solution

The effects of this temperature gradient on an optical wave passing through the material are determined by the phase change profile imparted by the gradient. In a normal lens, a phase change profile:

$$\Delta\phi = \frac{2\pi n}{\lambda}\Delta z \tag{7}$$

is imparted by differing path lengths, where n is the index of refraction, lambda is the wavelength of light passing through the lens and Δz is the difference in path length due to the shape of the lens. In the case of a plane parallel material where the index of refraction changes, the phase change profile is:

$$\begin{aligned}\Delta\phi_T &= \frac{2\pi}{\lambda} z\Delta n \\ &= \frac{2\pi}{\lambda} z\left(\frac{dn}{dT}\Delta T\right)\end{aligned} \tag{8}$$

If the 'thermal' accumulated phase change is equated to a perfect lens, which has a phase, where $r^2 = x^2 + y^2$, k is the wavenumber, and f is the focal length, of:

$$\Delta\phi_L = \frac{kr^2}{2f} \tag{9}$$

then the focal length of a thermal lens is:

$$\begin{aligned}\frac{kr^2}{2f} &= \frac{2\pi}{\lambda} z\left(\frac{dn}{dT}\Delta T\right) \\ \frac{r^2}{2f} &= z\left(\frac{dn}{dT}\Delta T\right) \\ \Delta T &= \left[2f\frac{dn}{dT}z\right]^{-1} r^2, \\ &= br^2 \\ f &= \left[2b\frac{dn}{dT}L\right]^{-1}\end{aligned} \tag{10}$$

where b is a quadratic fitting parameter, dn/dT is the differential change in refractive index with temperature, and L is the path length through the material. In the case of the face cooled materials, due to the rear reflection, L would equal $2L$. Using (10), the effective focal length of a one-dimensional slice taken from the temperature gradient surface at the origin and fit with a quadratic polynomial curve, as in Figure 17, could be calculated. The MatLab® program that was written to perform these steps can be seen in Appendix Two: MatLab Code, Listing 2: thermal_lens.m.

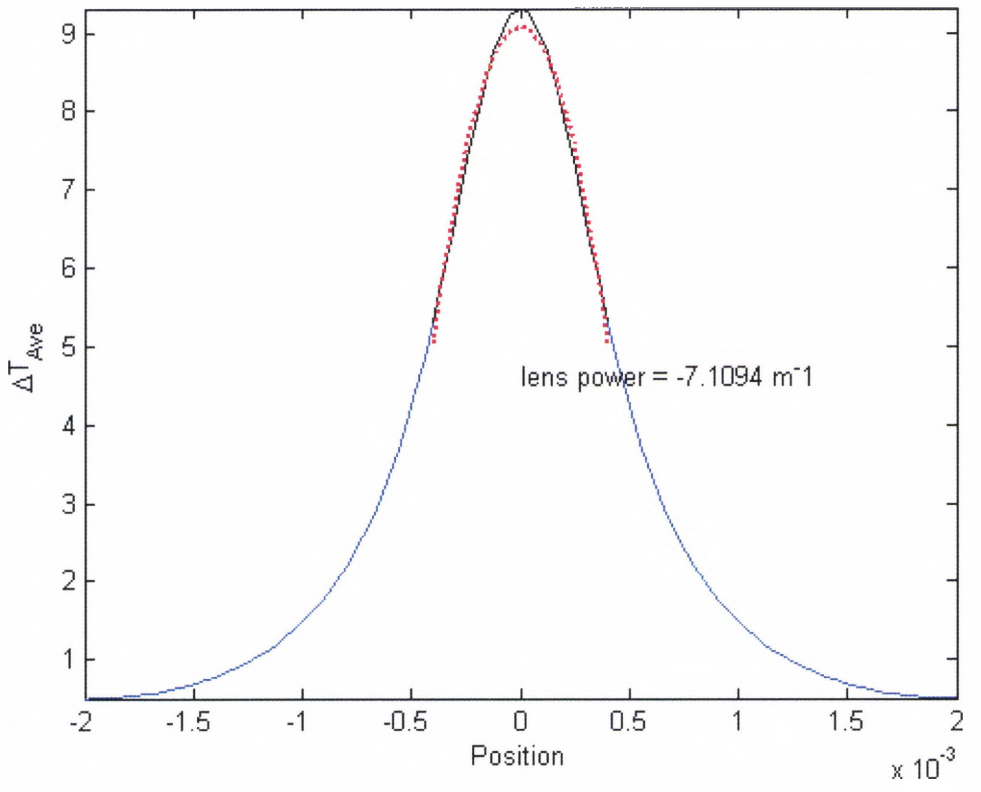

Figure 17: Quadratic lens fit for previous 4 mm face cooled thin disk surface

Of note in this last step is the choice of data window over which the curve is fit. All of the temperature profiles are more quadratic in the center of the data than at the edges, so as the diameter of fit is reduced, the curve fits a quadratic profile better. This fit diameter is analogous to the output laser diameter in the laser system that is being modeled. This is because only the portion of the temperature profile or lens that interacts with the output laser can contribute to changing its phase front, thus only that diameter should be considered in gauging its effective lensing power. In all models, the fitting window used was equal to the σ parameter of the pump beam.

4.3.1 Optimal transverse model dimensions

The first set of models run was intended to determine the maximum portion of the laser material geometry that needed to be included in the simulation. It was postulated that areas of the model farther from the center than approximately twice the pump beam radius would be irrelevant to the model solution and could thus be excluded. A set of basic face cooled models (modeled as parallelepipeds for simplicity) was constructed where the x and y dimensions varied from 2 mm to 8 mm while the pump beam σ was 0.4 mm.

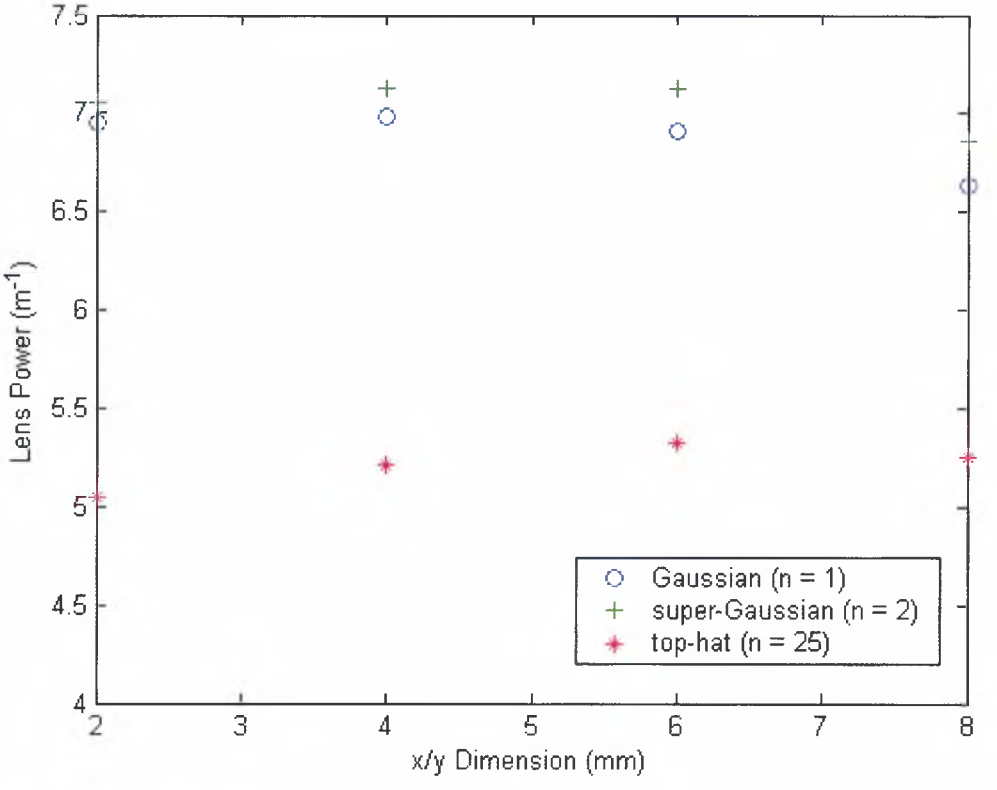

Figure 18: Variations in lens power with size

As seen in Figure 18, the thermal lensing power does not vary significantly with size and 4-mm sides will produce an upper bound on thermal lensing power. Figure 19 shows that the maximum average temperature rise levels off quickly starting with the 4-mm size. From these models, it was determined that the 4-mm x and y size was the optimal one to use.

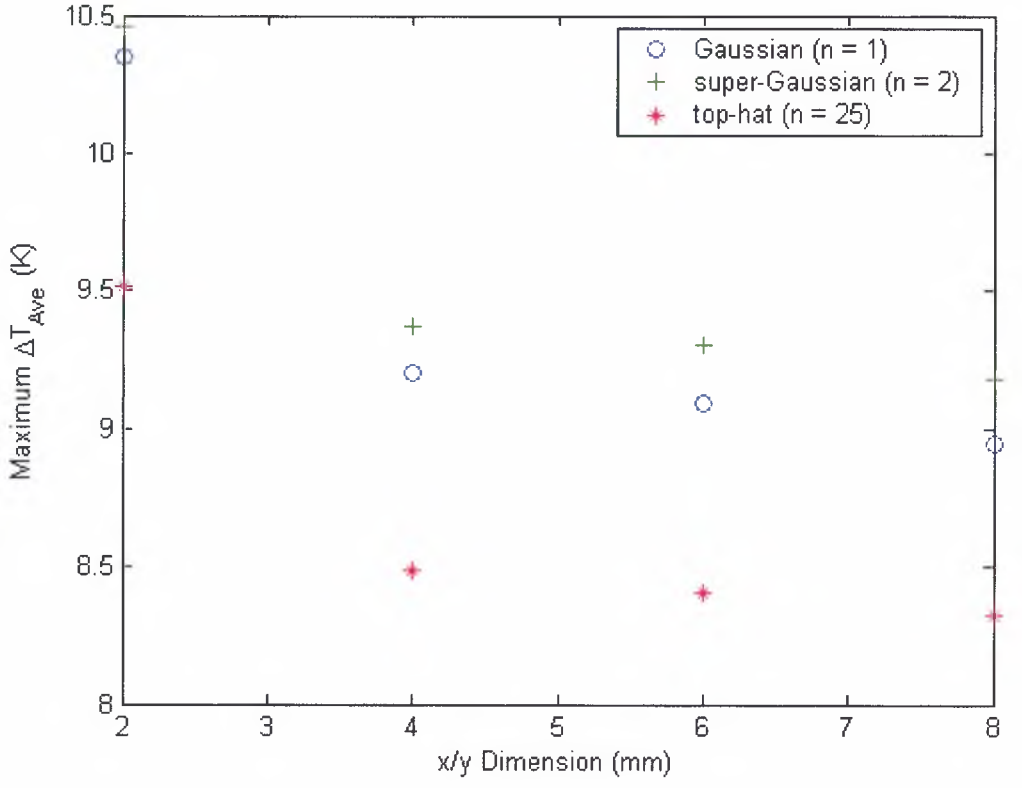

Figure 19: Variations in maximum average temperature rise with size

4.3.2 Optimal model complexity

Due to limited computer memory and CPU resources, it was desirable to run the models with as few degrees of freedom (a measure of the model complexity) as possible without sacrificing model quality. To insure that model complexity was not lowered to the point of affecting the results, the standard 4

mm model was run at varying degrees of freedom. The results, seen in Figure 20, show that the thermal lensing power leveled off quickly and that as long as some reasonable mesh size is chosen, the results would be acceptable. Figure 20 also shows the increasing amount of time that solving each level of complexity required. With FemLab®, solution time was not the main impediment however, memory consumption was. The most complex model that available computers could run was about 220000 degrees of freedom due to memory allocation issues.

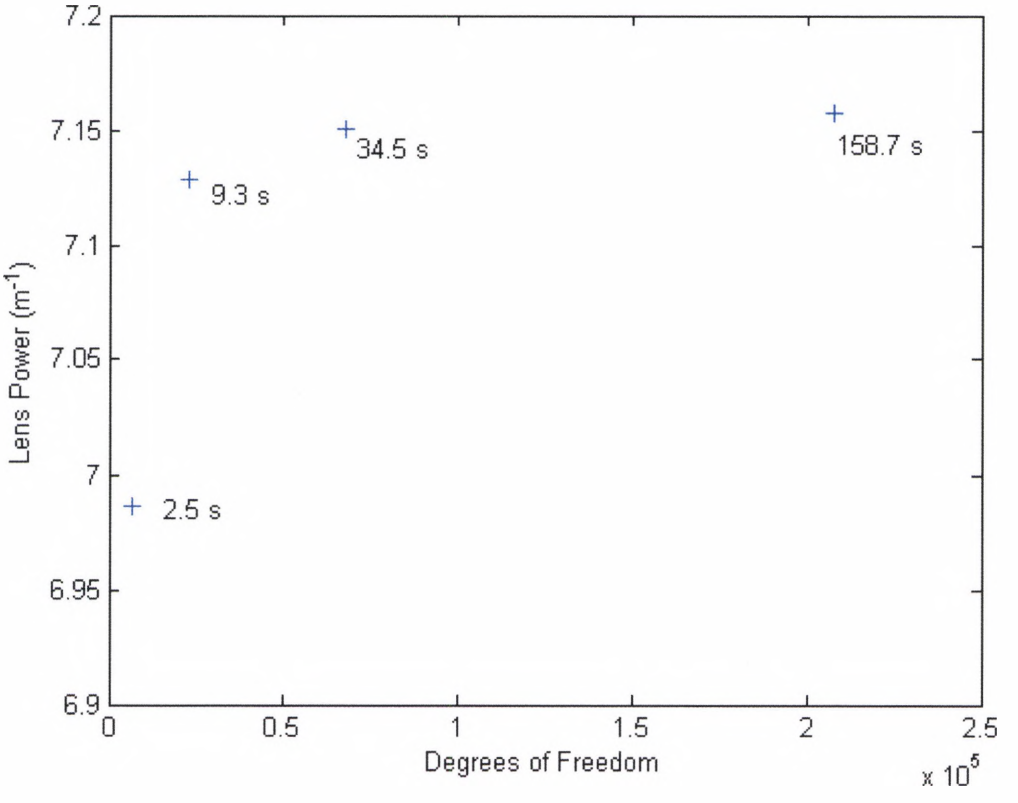

Figure 20: Effect of model complexity on thermal lensing power

4.3.3 Model symmetry properties

Once the appropriate x-y dimensions and model mesh complexity were established, the geometry of the sample itself was studied. Due to symmetry properties, it was beneficial to use thin cylinders instead of parallelepipeds in the models. A 4 mm diameter cylinder was compared to the 4mm by 4mm parallelepiped to gauge any differences. Figure 21, which shows the difference between the two geometries, has no clear pattern, but of note is that any differences in thermal lensing power between the disk and parallelepiped are two orders of magnitude smaller than the lensing power itself. This shows that the difference between the disk and parallelepiped geometries is negligible when looking at thermal lensing power.

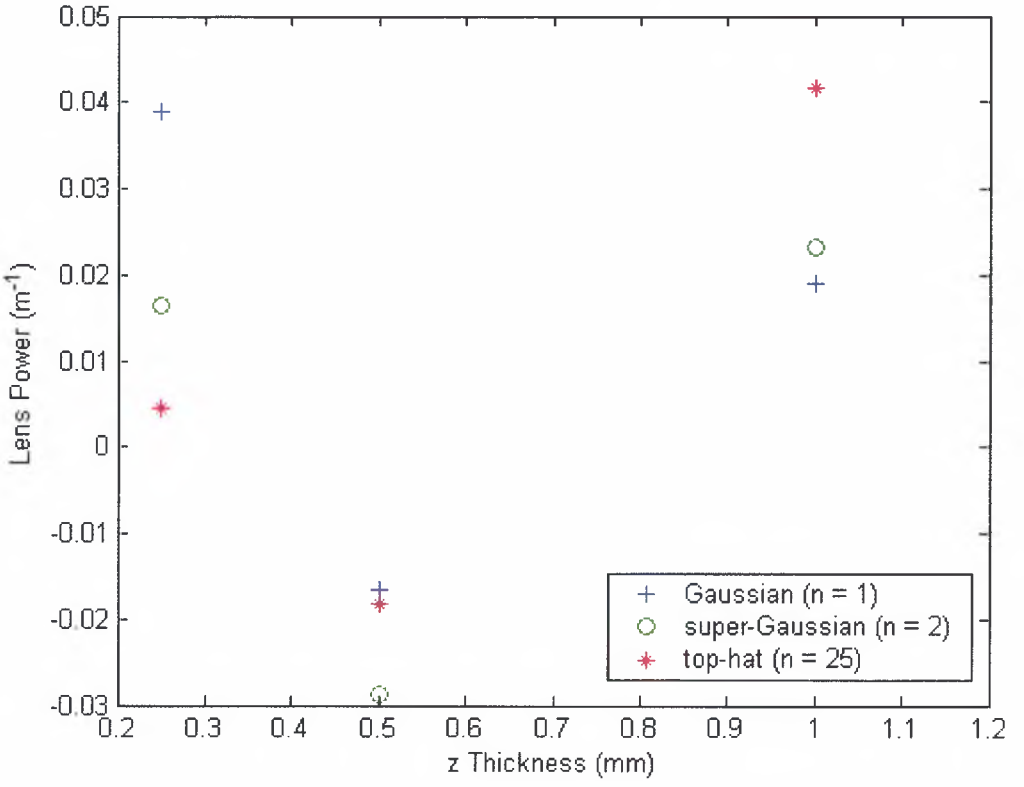

Figure 21: Difference in thermal lensing power between disk and parallelepiped

4.3.4 Variation with transverse thickness

In order to verify one of the tenets of the thin disk concept, namely that thermal lensing would scale with disk thickness, the effect of changing the z-dimension magnitude in the 4 mm diameter thin cylinder geometry was modeled. The results, seen in Figure 22, show that thermal lensing power should be proportional to thickness. It also shows that thermal lens power approaches an asymptote as the thin disk geometry approaches the traditional rod geometry.

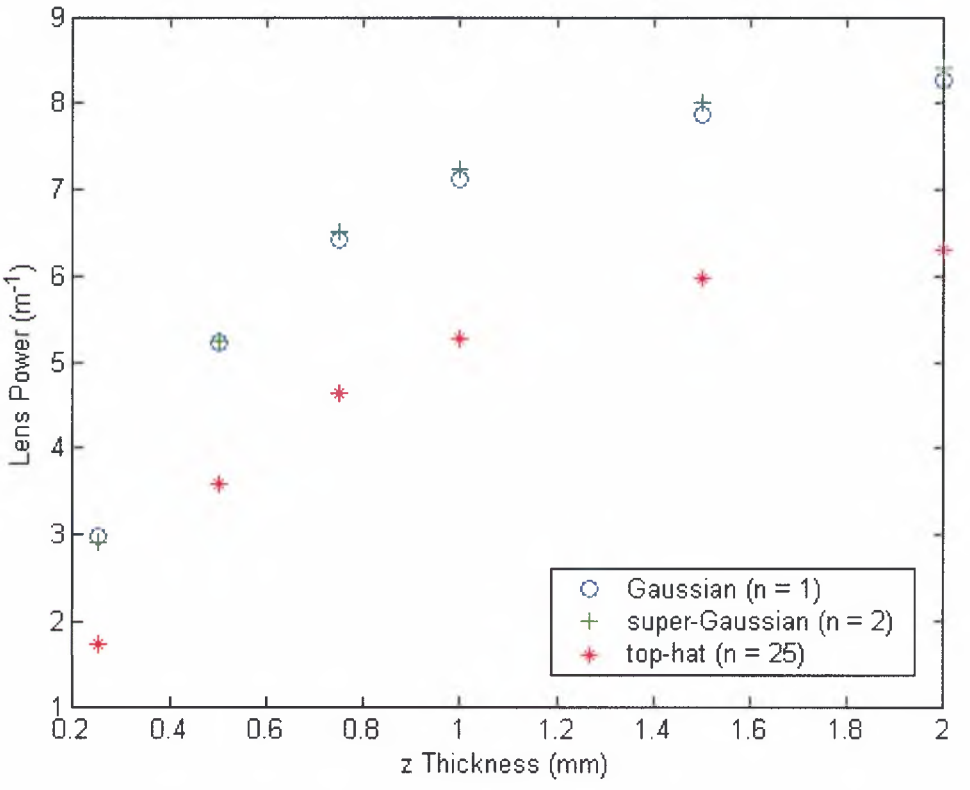

Figure 22: Variation in thermal lens power with thickness

4.3.5 Cooling configuration variations

Finally, the thermal lens power and maximum temperature rise for the proposed thermal issue mitigation designs were modeled for the 4 mm diameter thin cylinder geometry with a Gaussian (n = 1) pump beam with a σ of 0.4 mm. The temperature distributions of these simulations can be seen in Figure 15 as well as Figure 23 through Figure 26. The results from processing the data for these models can be seen in Table 3. The calculated thermal lens power and maximum temperature increase were essentially identical for the basic face cooled and ring and face-cooled designs. The ring and face-cooled design with window showed a marked temperature benefit of 44% lower than the basic face

cooled thin disk model. The pass-through pumped design exhibited 38% stronger thermal lensing and 89% higher maximum temperature increase with respect to the basic face cooled thin disk model, clearly not a desirable outcome. The pass-through pumped design with dual windows had 33% stronger thermal lensing, but the benefit of 21% lower maximum temperature increase, again with respect to the basic face cooled thin disk model.

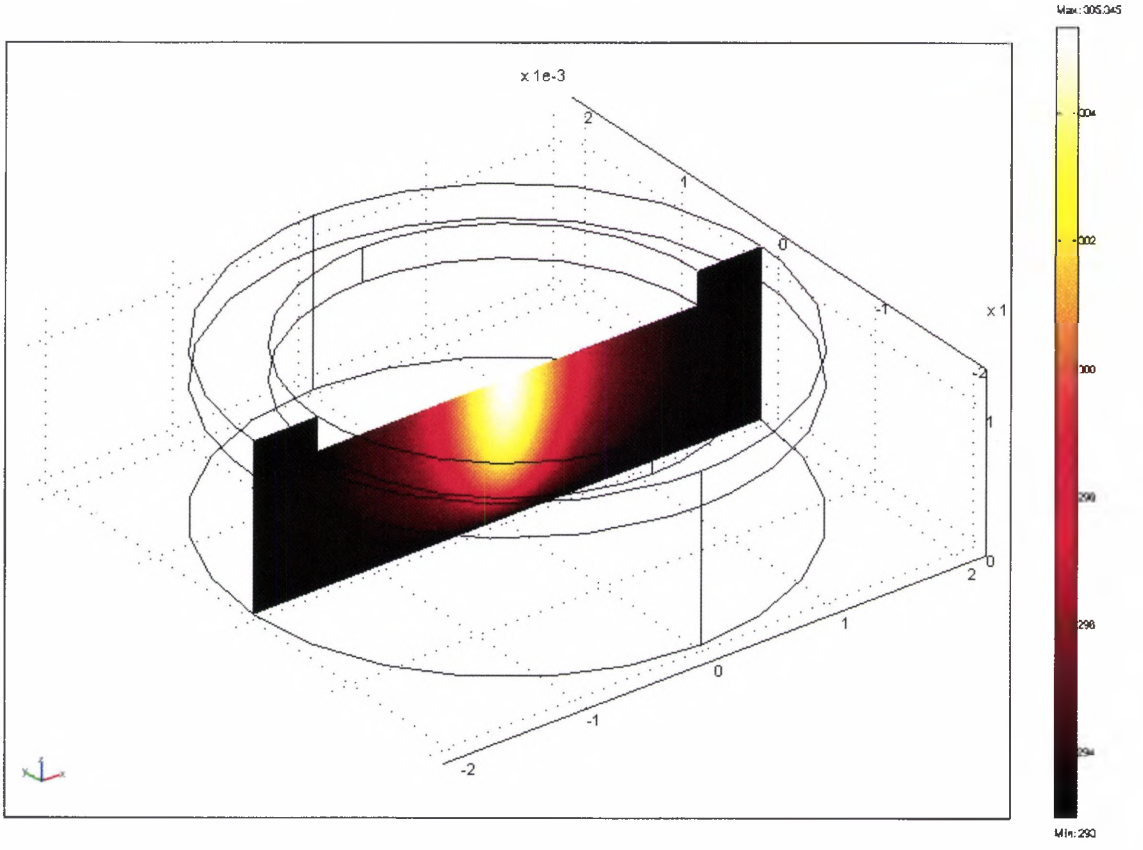

Figure 23: Simulation solution of 4 mm diameter, 1 mm thick ring and face cooled thin disk pumped with a Gaussian (n = 1) beam with σ = 0.4 mm

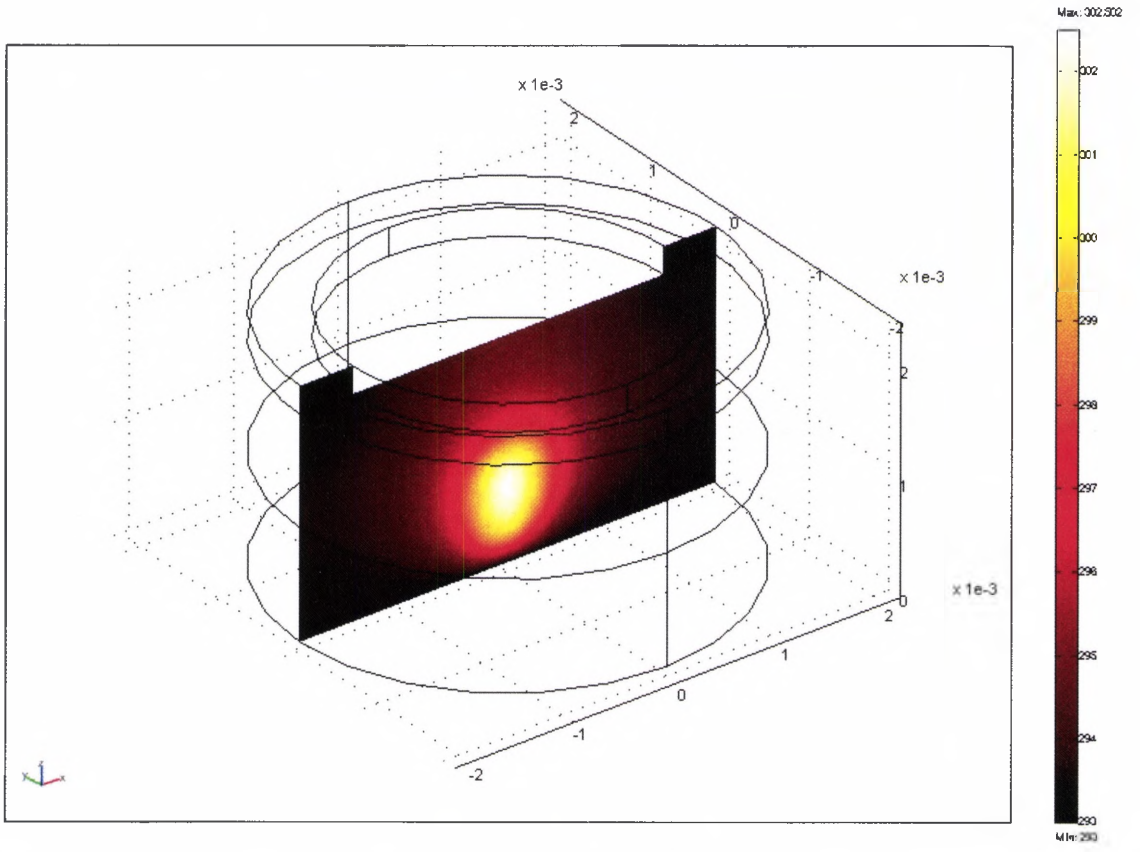

Figure 24: Simulation solution of 4 mm diameter, 1 mm thick ring and face cooled thin disk with window pumped with a Gaussian (n = 1) beam with σ = 0.4 mm

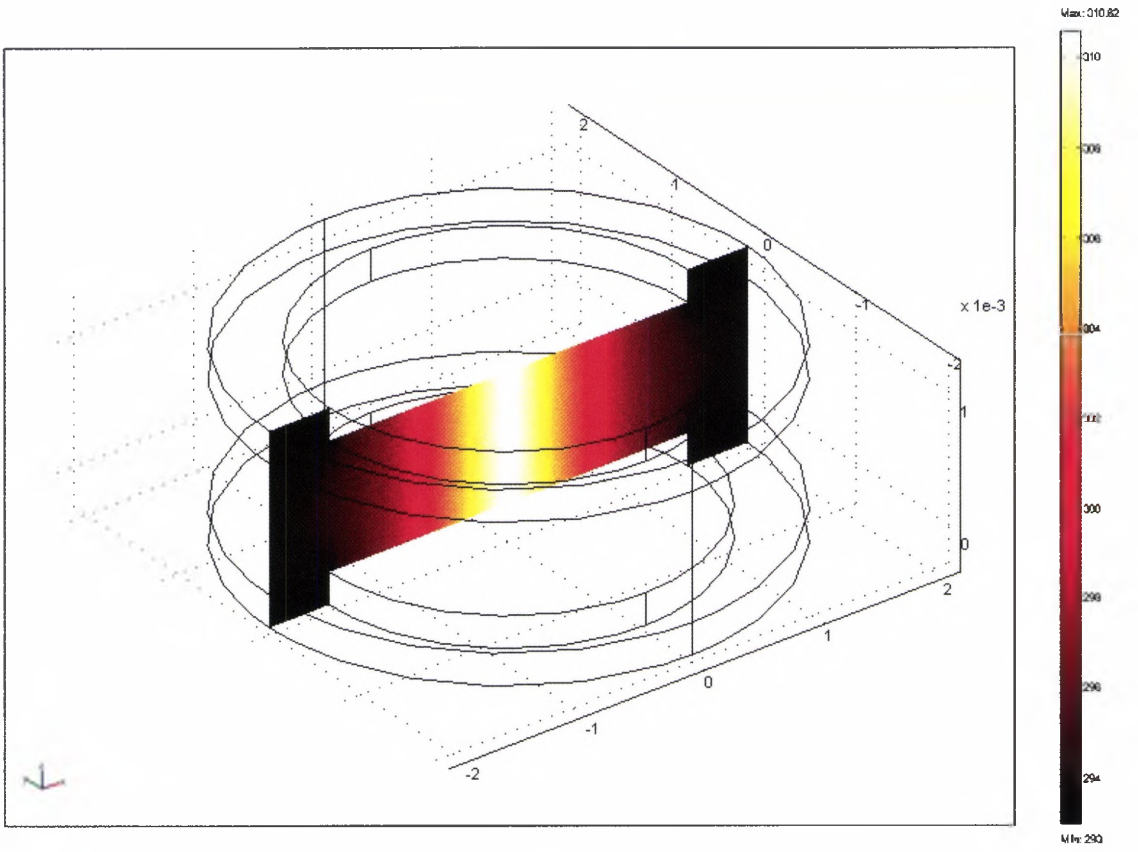

Figure 25: Simulation solution of 4 mm diameter, 1 mm thick pass-through pumped thin disk pumped with a Gaussian (n = 1) beam with σ = 0.4 mm

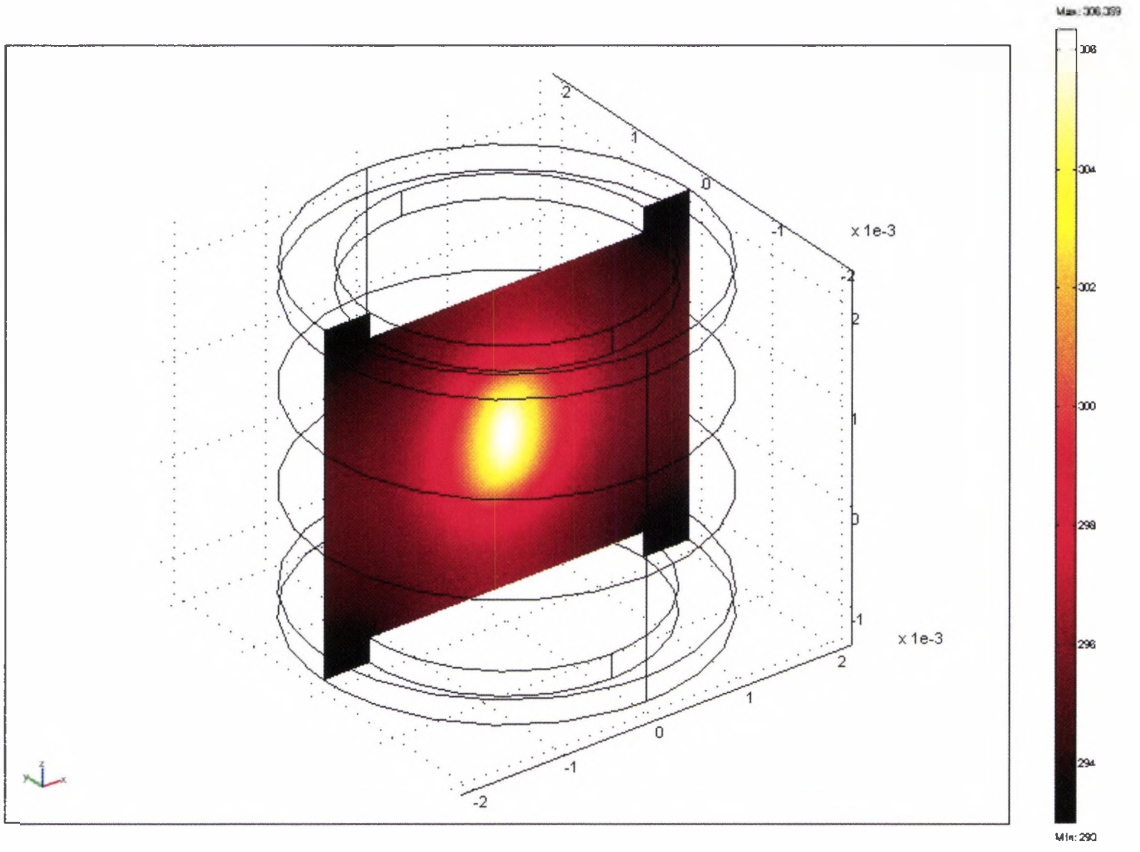

Figure 26: Simulation solution of 4 mm diameter, 1 mm thick pass-through pumped thin disk with dual windows pumped with a Gaussian (n = 1) beam with σ = 0.4 mm

Table 3: Predicted results for thermal issue mitigation methods

Model	Predicted Thermal Lens Power (m^{-1})	Max Ave Temp Rise (K/W)	% Lens Power Difference	% Max Ave Temp Difference
Basic Face Cooled	7.11	9.31	-	-
Ring / Face Cooled	7.14	9.16	0.5	-2
Ring / Face Cooled with Window	7.19	5.21	1	-44
Pass-Through Pumped	9.81	17.61	38	89
Pass-Through Pumped with Dual Windows	9.48	7.39	33	-21

4.4 Modeling conclusions

The models indicated the best approach to take during the experimental phase of the research was to focus on the pass-through pumping scheme with dual windows. While this design does have higher thermal lensing than the basic face cooled design, it would still be an improvement over traditional designs due to the practical considerations such as construction and coating issues. In addition, the overall temperature rise in the design was substantially lower, possibly allowing the laser to be force air-cooled as opposed to needing water cooling, a definite advantage in light of the larger goals of mid-IR laser

source development. The overall temperature rise also will have a direct effect on the efficiency of the laser due to the fact that the excited state lifetime decreases quickly for temperatures above 300 K.[14]

Chapter 5
Final Laser Design

After the type of cooling design was decided upon, it was necessary to develop a final laser design for construction. It was decided to use a confocal cavity arrangement because this would allow for easier alignment of the cavity as well as allowing more room for the sample holder in the cavity. In the final laser design, seen in Figure 27, the pump beam was directed into the cavity by a high reflectivity turning mirror. The confocal cavity itself consisted of 20 cm radius of curvature zinc selenide mirrors coated AR from 1.9 to 2.1 μm. One mirror was coated to be HR from 2.5 to 3 μm and there were a variety of outcoupler reflectivies used for the other mirror. A turning mirror that was coated to selectively reflect the laser wavelengths while passing the pump wavelengths at a 45˚ angle of incidence was used to separate the two beams after the cavity. A long-pass filter was used to prevent any wavelengths below 2.07 μm from reaching the laser detector and camera.

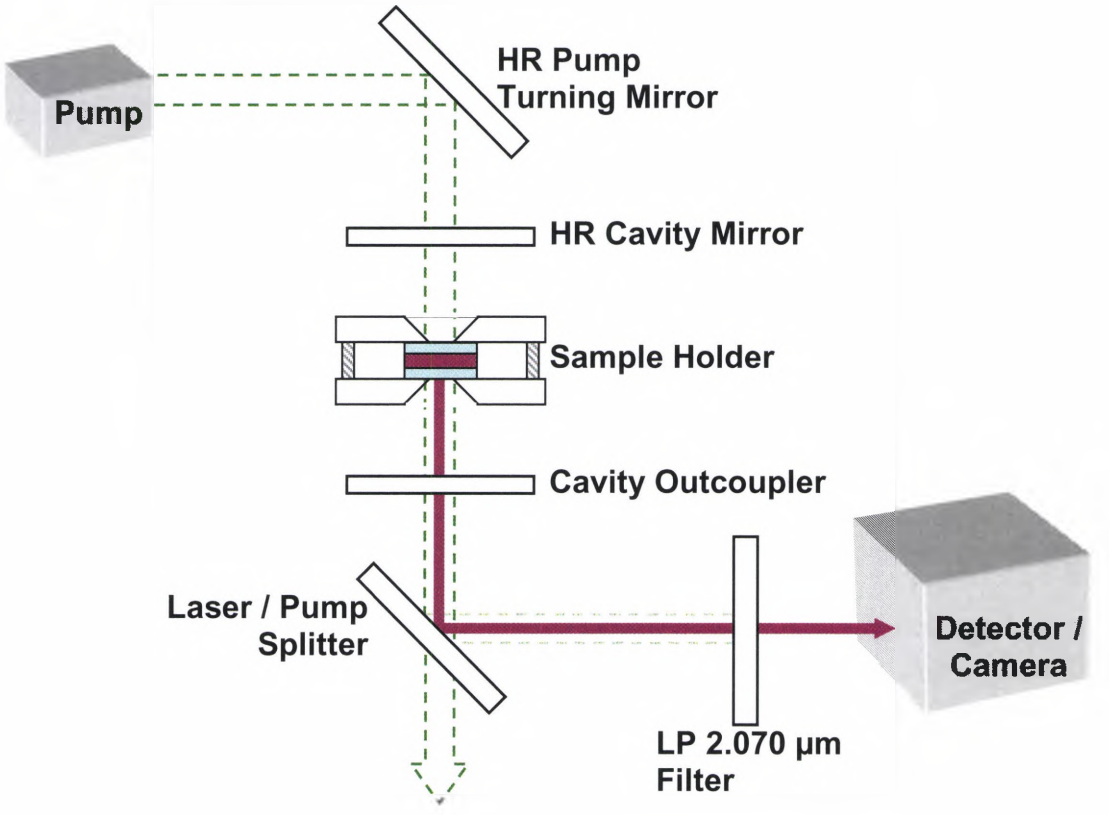

Figure 27: Final experimental pass-through laser design

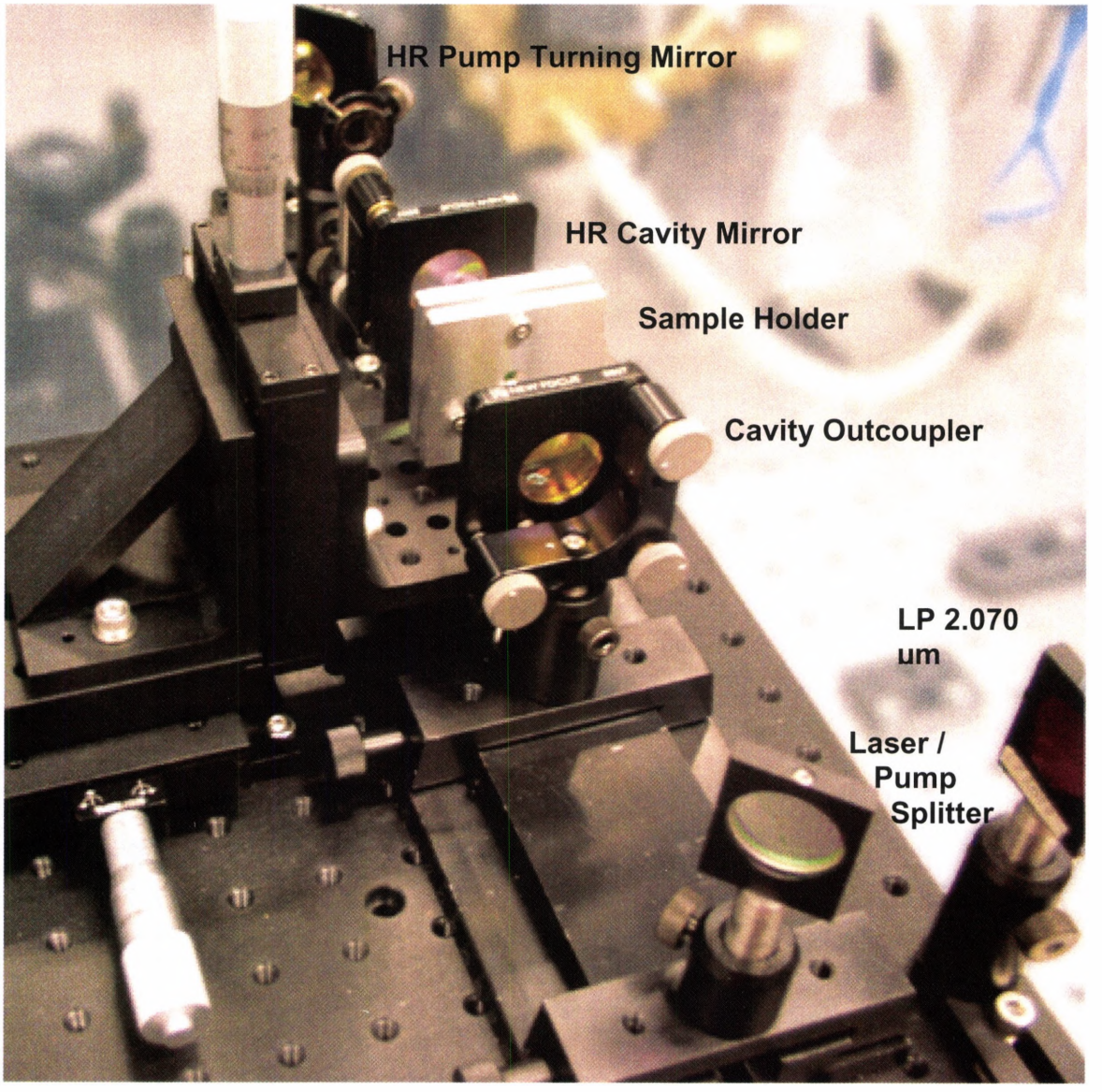

Figure 28: Pass-through pumped thin disk laser with dual windows

The next step in constructing the laser was to design and fabricate the sample holder itself. The dual-window sample holder had to be able to hold the two undoped windows and have an adjustable tensioning system in order to hold the laser sample between the windows. It also needed to have an opening for the pump beam to pass though the system without vignetting. The first dual-window sample holder was designed to be water cooled and had two channels in

each side to accommodate the cooling water flow. It used four standard nuts and bolts to tighten the two sides together. This design can be seen in Figure 29 and the fabricated sample holder can be seen mounted in Figure 30 and open in Figure 31 along with two undoped windows and sample CR44.

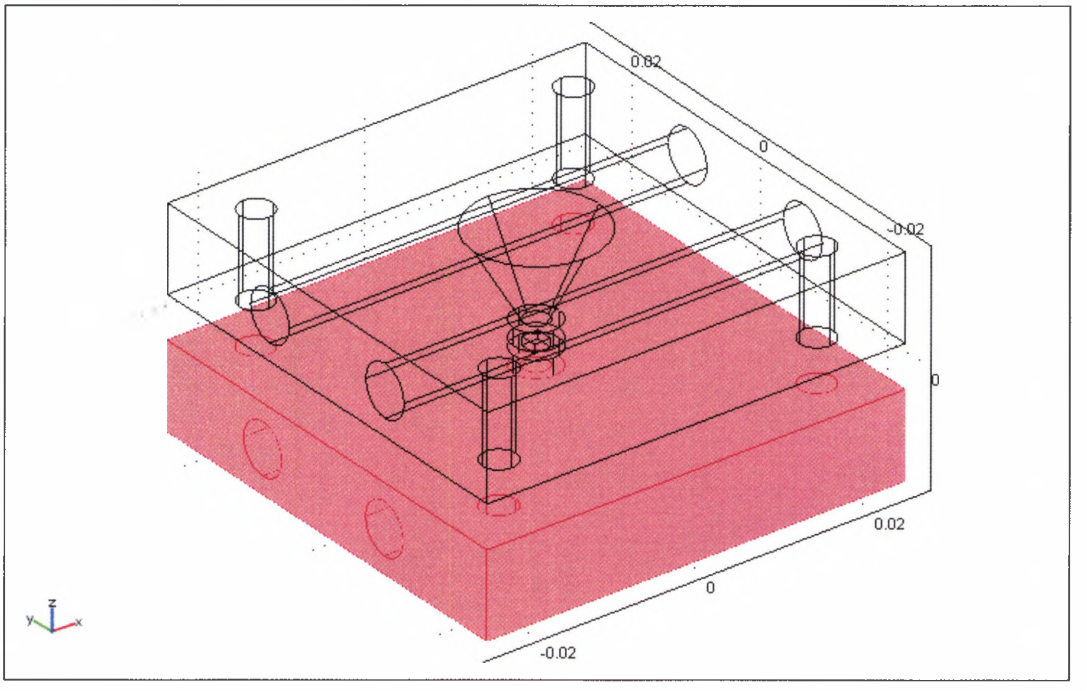

Figure 29: CAD design of water-cooled dual window sample holder

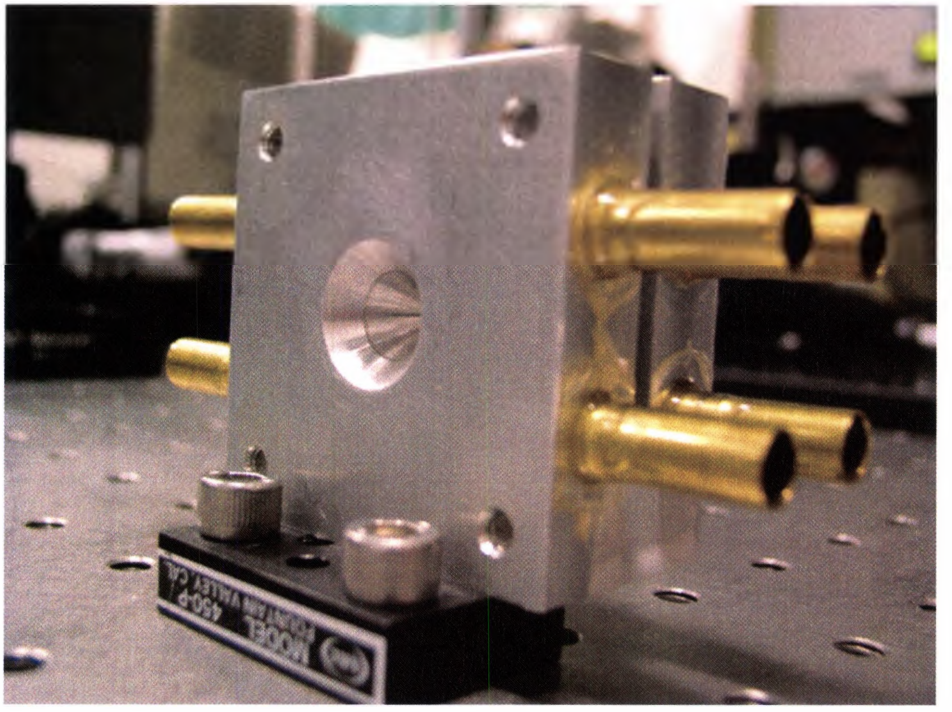

Figure 30: Water-cooled dual window sample holder

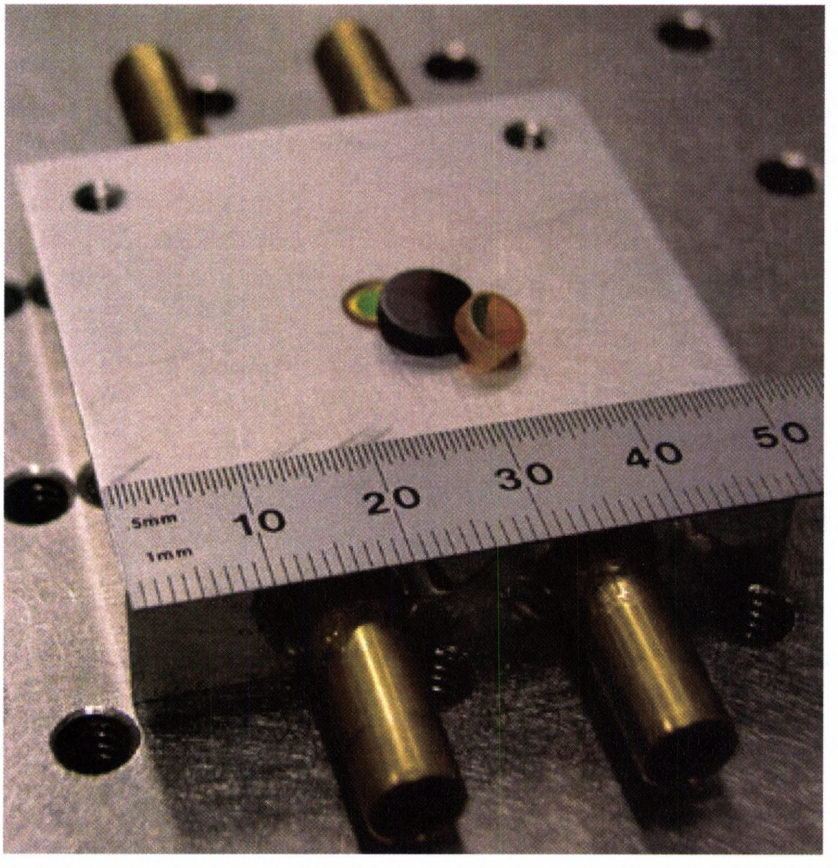

Figure 31: Water-cooled dual window sample holder open with windows and sample CR44

The water-cooled dual window sample holder had some sight flaws in its design. The tensioning system used rather coarse threaded bolts which made fine adjustments during tightening risky to the windows or laser sample. In addition, water cooling was not going to be used during this research, so that feature of the sample holder added unneeded complexity and size to the design. A second sample holder was designed and fabricated which used three finely threaded posts and thinner heat sink walls. The design for this version can be seen in Figure 32 and the fabricated sample holder in Figure 33. This sample holder was used throughout the experimental portion of the research.

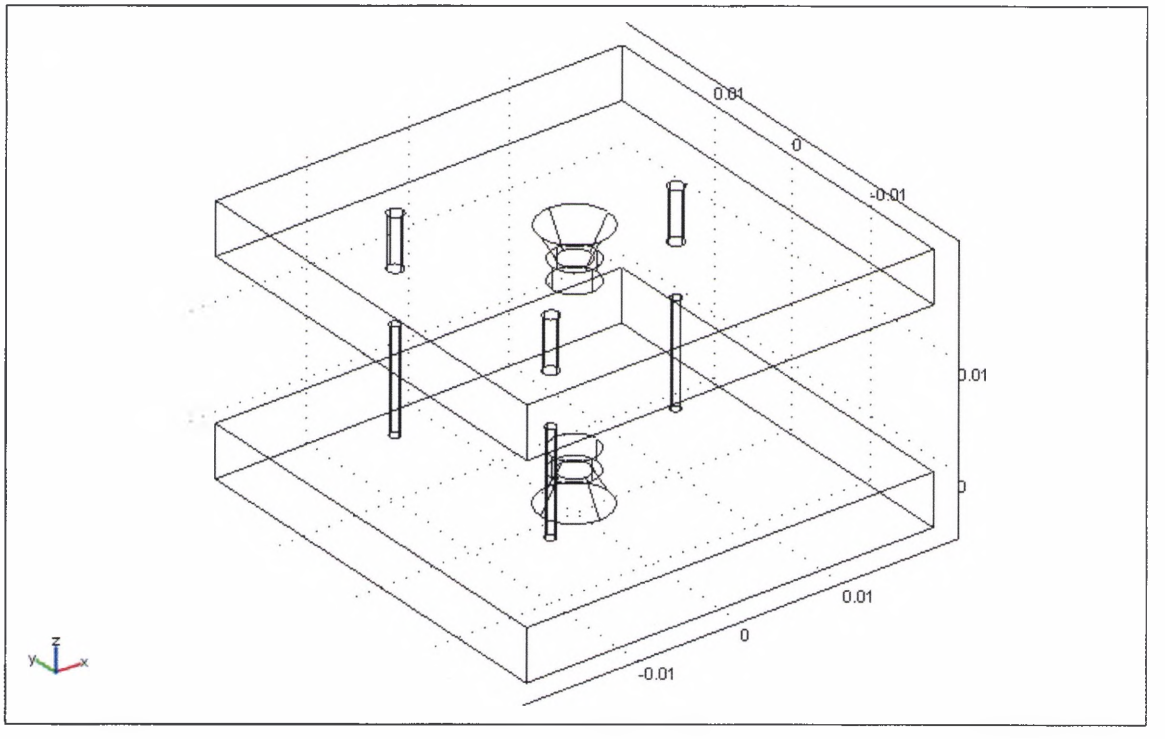

Figure 32: CAD design for dual window sample holder MkII

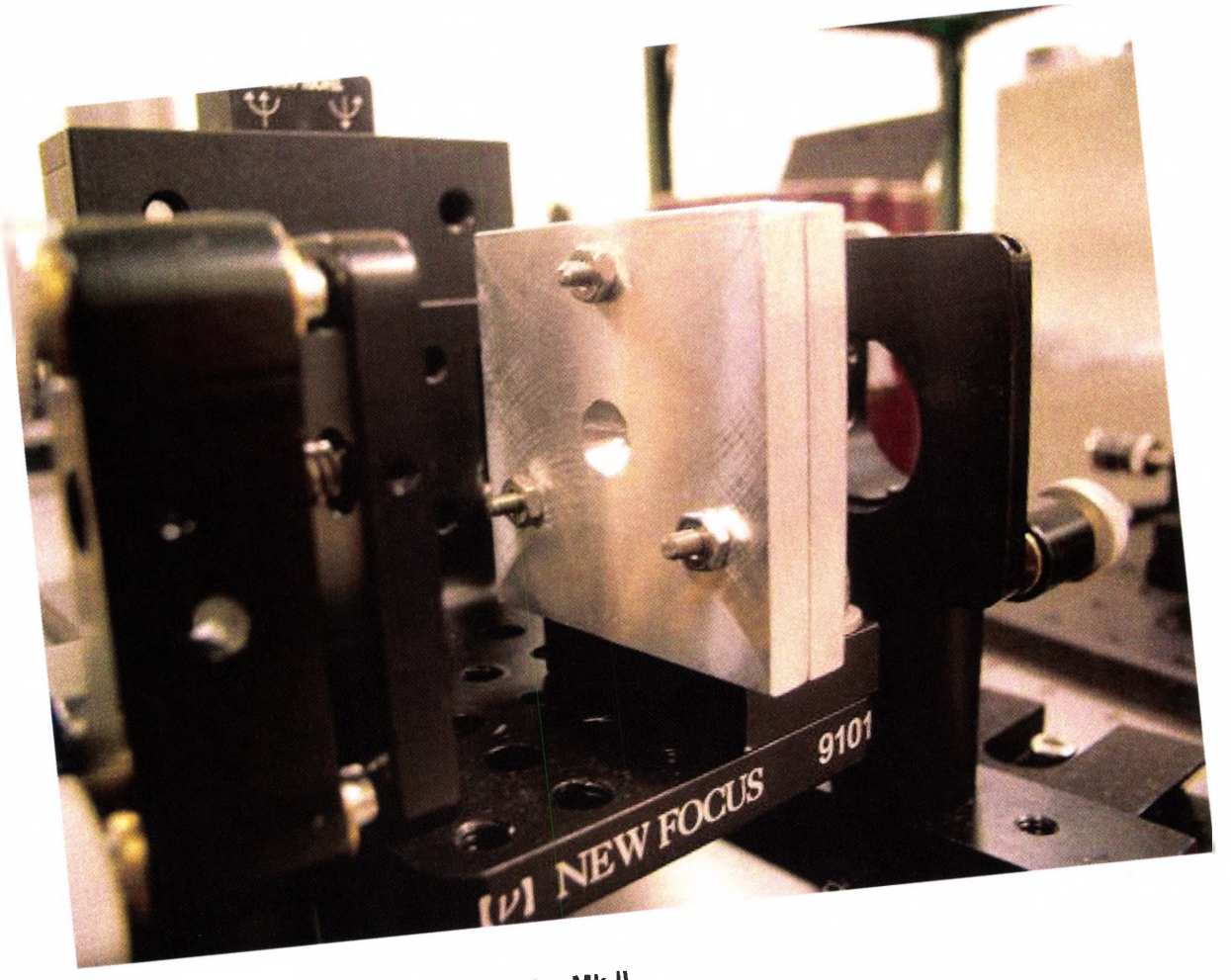

Figure 33: Dual window sample holder Mk II

Chapter 6
Pump Sources

Two different pump sources were used in this research. The majority of the research was to be carried out using a pulsed laser, but it was also important to attempt pumping with a CW source as well. The following sections give a brief description of each pump source.

6.1 Pulsed Tm:YLF

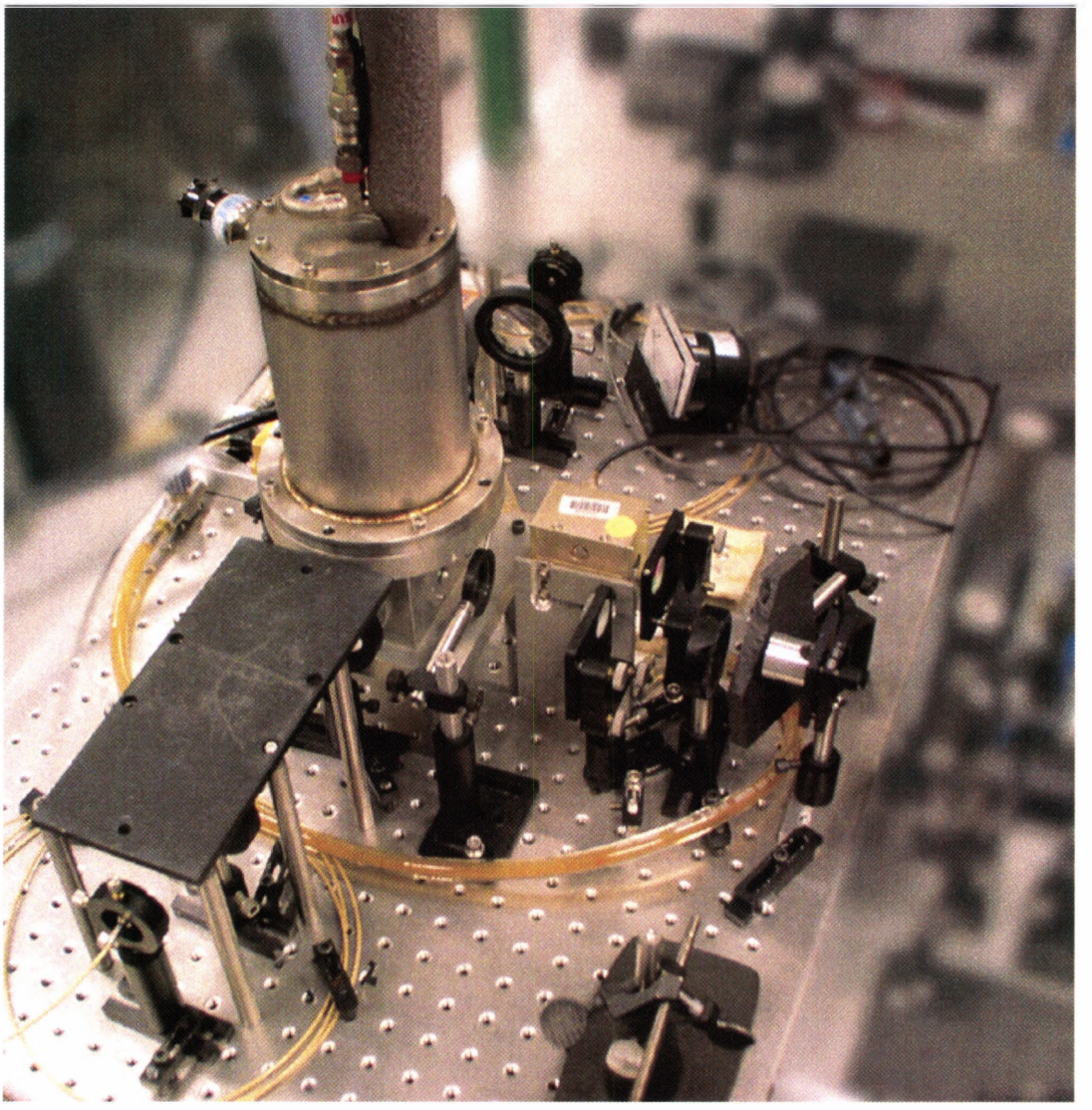

Figure 34: Pulsed Thulium Yttrium Lithium Fluoride (Tm:YLF) laser

The pulsed thulium yttrium lithium fluoride (Tm:YLF) laser, seen Figure 34, was Q-switched and could be run at pulse repetition frequencies (PRF) of 10 kHz to 50 kHz. At the upper limit of PRF, the laser would behave somewhat erratically, occasionally missing pulses. This laser had a maximum average power output of approximately 8 W at a wavelength of 1.89 μm.

6.2 40W Tm Fiber

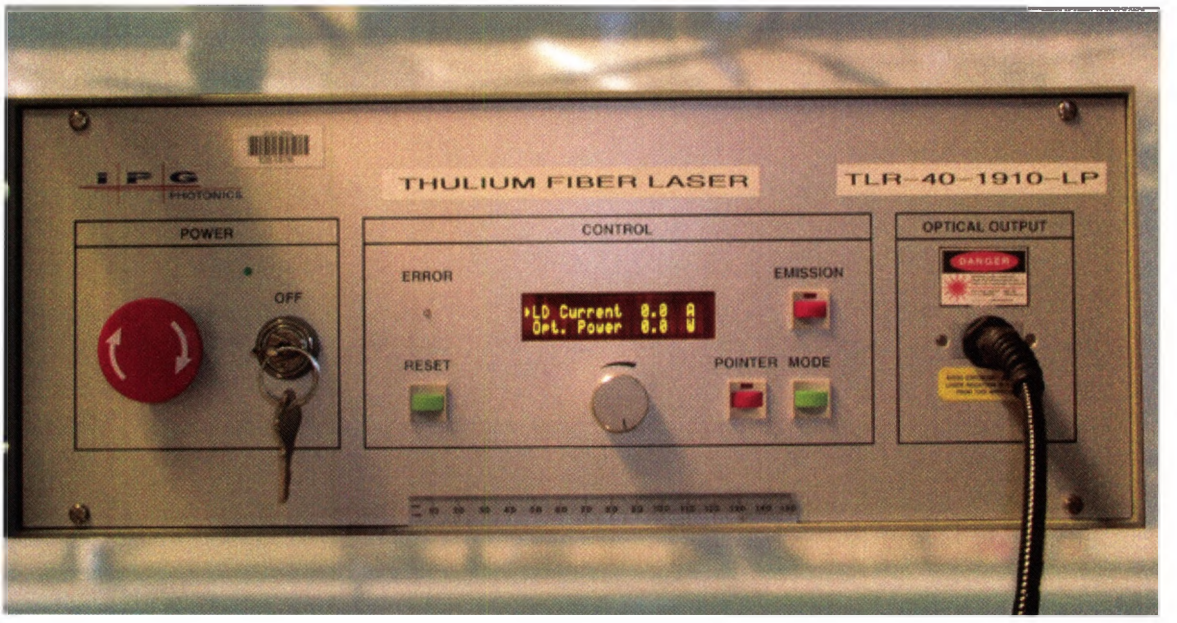

Figure 35: Thulium (Tm) fiber laser

For CW pumping, a thulium fiber laser was available. This laser had a maximum power output of 40 W at 1906.2 nm. This laser could also be run at modulated duty cycles up 2 kHz if needed.

Chapter 7
Thermal Lensing Mitigation Experiments

In the experimental portion of the research, a number of goals were achieved. First, a number of baseline measurements were made to pave the way for the thermal lensing experiments. Then variations in cavity length were studied to determine optimal size of the cavity. Losses in the cavity were studied and finally thermal issues were investigated.

7.1 Baseline Measurements

In order to measure the slope efficiency of the laser, the power output would be plotted versus the power absorbed by the sample. To determine the amount of power absorbed by the sample (assuming no losses due to the undoped windows and their interfaces), the power passing through the sample was subtracted from the power incident on the sample. To measure these two quantities, the average transmission percentage was measured from point *A* to point *B* (T_1, the fraction of pump power incident on the front zinc selenide window) and from point *C* to point *E* (T_2, the percent transmission at the pump wavelength of the rear half of the optics train) in the cavity diagram seen in Figure 36. This was done because points *A* and *E* are the most accessible measurement points. The power absorbed was then calculated using (13),

below. The average value for T_1 was 86.05%±0.3%, the average value of T_2 was 66.54%±1.4%.

$$T_1 = \frac{B}{A} \Rightarrow B = T_1 A \tag{11}$$

$$T_2 = \frac{E}{C} \Rightarrow C = \frac{E}{T_2} \tag{12}$$

$$P_{ABS} = B - C = T_1 A - \frac{E}{T_2} \tag{13}$$

The output power of the laser was measured at point *F*, behind a 2.070 µm long pass filter, so as to block any portion of the pump reflected from the pump/laser beam splitter. The average transmission percentage from point *D* to *F* (T_3, the effective transmission at the laser wavelength of the rear half of the optics train) was 62.88%±0.9%. This allows the calculation of the output power of the laser using (14) below.

$$P_{OUT} = \frac{F}{T_3} \tag{14}$$

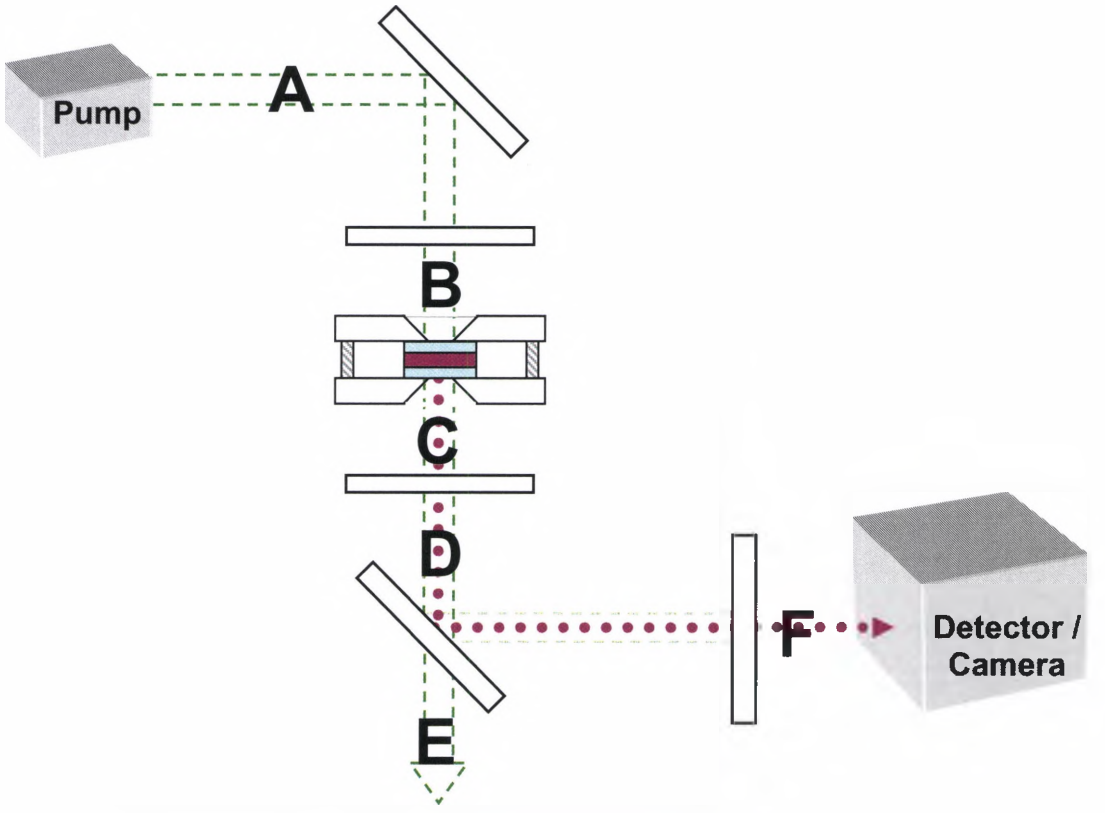

Figure 36: Measurement positions in laser cavity

7.2 Cavity Length Variations

As mentioned in Chapter 5 Final Laser Design, the cavity mirrors in this design were 20 cm radius of curvature. This would mean that cavity lengths up to 20 cm should be stable, if no thermal lensing is present. In order to examine the effect of cavity length variation on the stability of the cavity, the slope efficiencies for different cavity lengths were measured for sample CR44 at a pulse repetition frequency (PRF) of 10 kHz and an outcoupler reflectivity of 99%. The slope efficiencies were calculated using the adjusted transmission values collected in previous section. These experiments clearly showed that, within the experimental parameters,

slope efficiency was linearly proportional to cavity length with a negative slope. This trend can be seen in Figure 37.

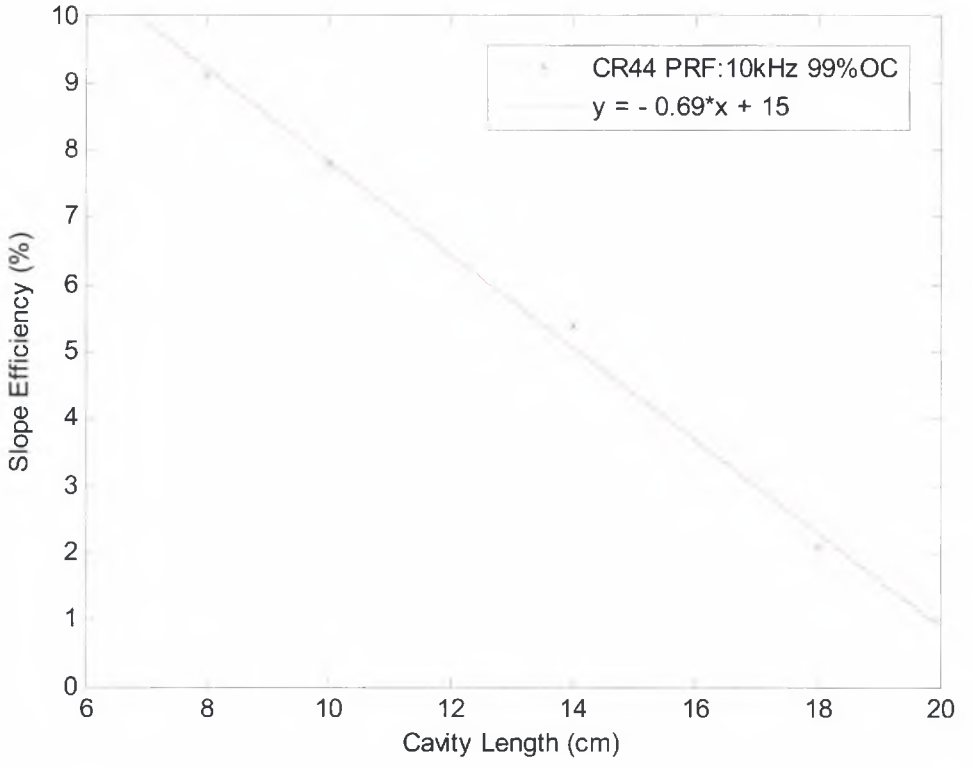

Figure 37: Slope efficiency variation with cavity length

7.3 Determining Cavity Losses

One of the hurdles to constructing a laser has always been limiting the cavity losses, specifically the losses at the laser medium surfaces. Traditionally this is achieved by having the surfaces AR coated, an expensive and time consuming process. In the pressed surface laser design, the laser gain medium was clamped between two undoped zinc selenide windows, both of which were AR coated on their outer faces and uncoated on their inner faces. This allowed any number of uncoated laser samples to be used with a set of pre-made AR

windows. The losses in this arrangement were theoretically only limited by the quality of the AR coatings, assuming a perfect interface between the inner faces of the windows and the laser gain medium. However, in practice, the losses were determined by how well the windows and gain medium can be clamped together in addition to how well the interfacing surfaces have been plane-parallel polished. In general, the tighter that the three pieces can be clamped, the lower the losses were. The practical limit to this was the mechanical fracture point of the windows. Thus, a fine line existed between acceptable losses and broken windows. Fortunately, due to the design of the sample holder, it was always a replaceable window that cracked before the much more valuable laser sample.

To determine the cavity losses in the pressed surface laser using Findlay-Clay analysis, the slope efficiencies were measured as a function of outcoupler reflectivity. Using sample CR44 and a pulse repetition frequency (PRF) of 10 kHz, the slope efficiency was measured using 99, 95, 75 and 50 percent reflective outcoupler mirrors. A plot of the negative natural log of the outcoupler reflectivity versus threshold power can be seen in Figure 38. Using this and (15) we can determine the round-trip losses in the cavity.[15] In this equation, R is the outcoupler reflectivity, K is the slope of the line, P_{TH} is the threshold power and L is the round-trip resonator loss.

$$-\ln R = 2KP_{TH} - L \tag{15}$$

The round-trip losses for this cavity were 22%, which is a single-pass loss of 11%. This compares very favorably to the theoretical single-pass loss of 32%

for Fresnel losses on non-windowed laser medium (using an index of refraction for zinc selenide of 2.44 at 2.5 μm).[16]

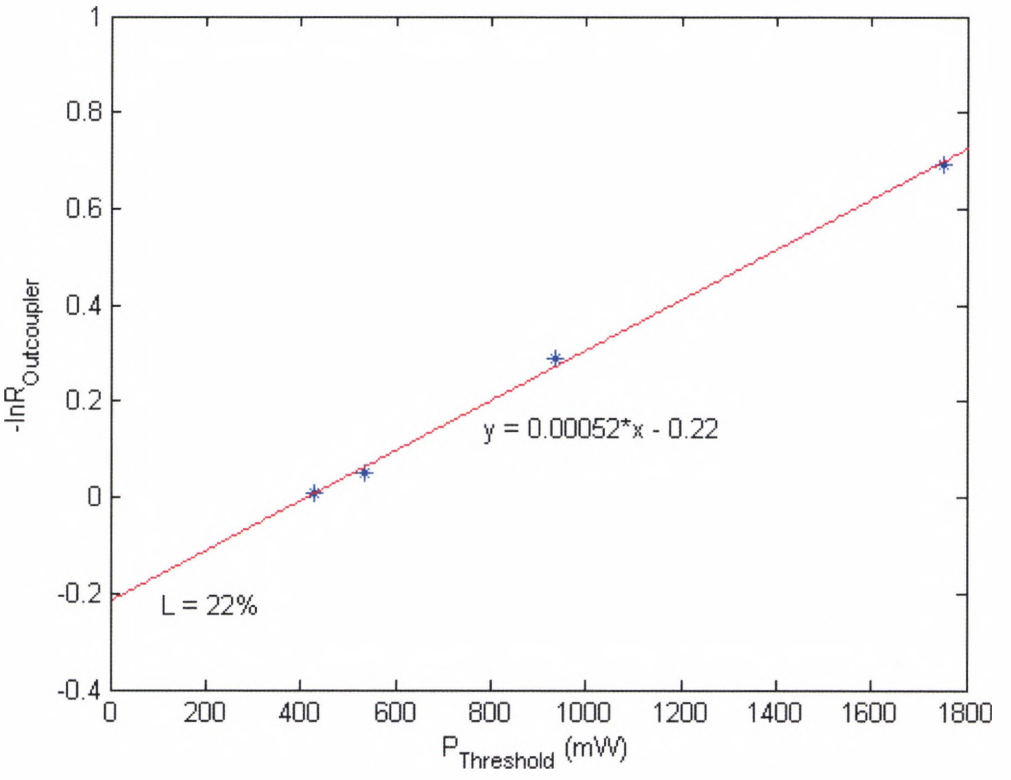

Figure 38: Findlay-Clay analysis of CR44 laser cavity

Findlay-Clay analysis was also performed in the same manner using samples CR48 and CR49. The slope efficiencies were measured for 99, 95 (CR49 only) and 75 percent reflective outcoupler mirrors. This data can be seen in Figure 39 and Figure 40. The CR48 cavity had round-trip losses of 47% and the CR49 cavity had round-trip losses of 45%. These losses (around 23% single-pass) still compare favorably to the theoretical Fresnel loss of 32%, but are definitely not optimal.

The higher losses seen in the CR48 and CR49 laser cavities could arise from two different sources. One possibility is that of imperfect surface mating. It

is possible in both experiments that the sample holder was not tightened properly, there were particles between the windows and the laser medium, the surfaces of the laser samples were not plane-parallel polished properly or any combination of these. Losses due to foreign particles were minimized by assembly in a clean environment and the sample holder was clamped in a steady, deliberate manner each time, so the contributions of these types of problems to the losses should be minimal. Another possibility is that these samples had a higher scattering loss than did CR44. Samples CR49 and CR49 had measured lifetimes of 2.24 μs and 3.86 μs respectively, whereas CR44 had a measured lifetime of 4.77 μs. This would indicate that the concentration of chromium in samples CR48 and CR49 is much higher than that in CR44. It is likely that both poor polishing and scattering contributed to the higher losses.

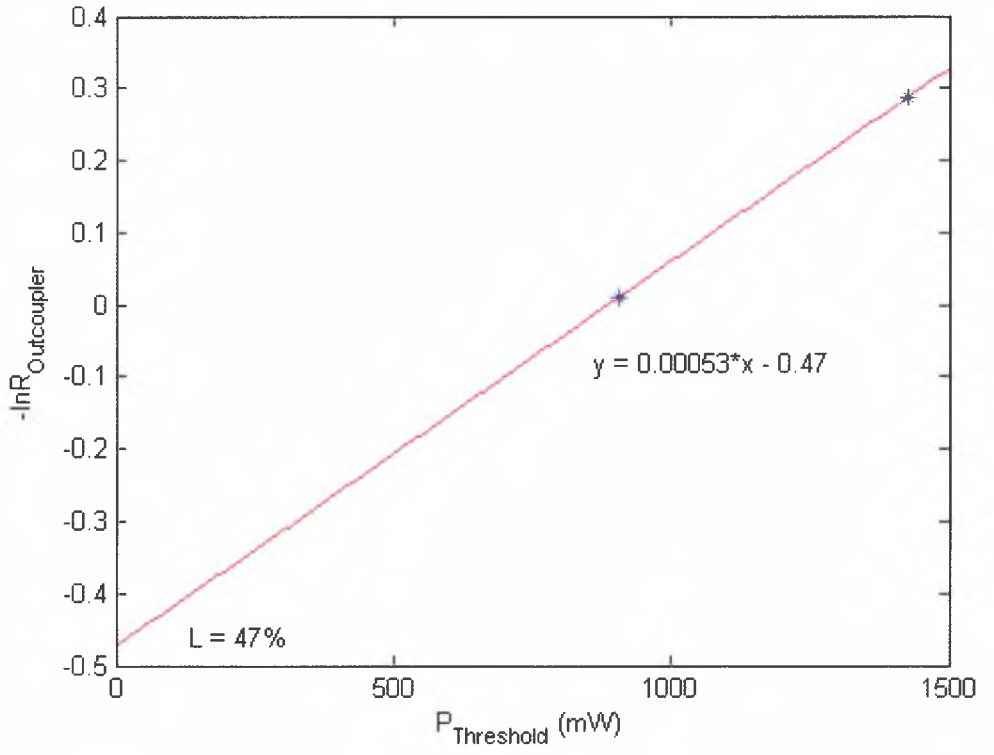

Figure 39: Findlay-Clay analysis of CR48 laser cavity

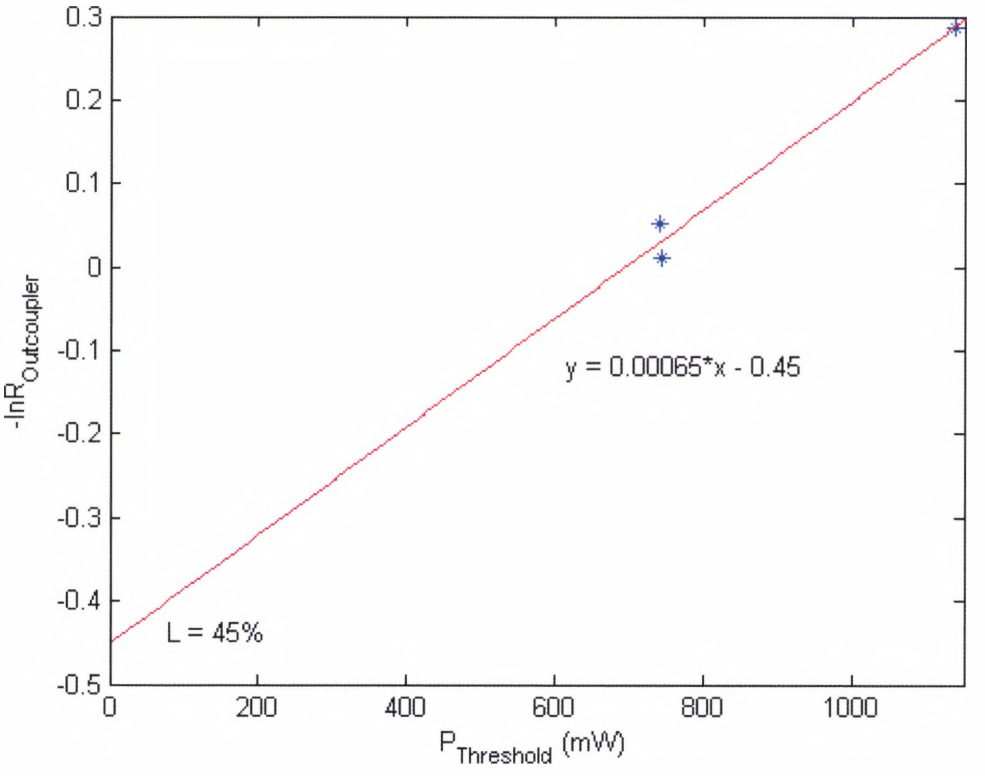

Figure 40: Findlay-Clay analysis of CR49 laser cavity

7.4 Thermal Effects Investigation

It is important to note that, in the above experiments, the slope efficiency plots, with one exception, showed no thermal lensing effects to be present. An example can be seen in Figure 41, which shows the slope efficiency for CR49 with an 8 cm cavity using a 99 percent reflective outcoupler. In contrast, the slope efficiency plot for CR48 at a PRF of 10 kHz and a 75 percent reflective outcoupler, seen in Figure 42, had a noticeable non-linearity at higher powers. Thermal lensing would typically be indicated in a slope efficiency plot by a decrease in the power output at the higher input powers.[17] In this case, the power input was high enough to cause enough thermal lensing to destabilize the

laser cavity, decreasing the output power. This result merited further investigation.

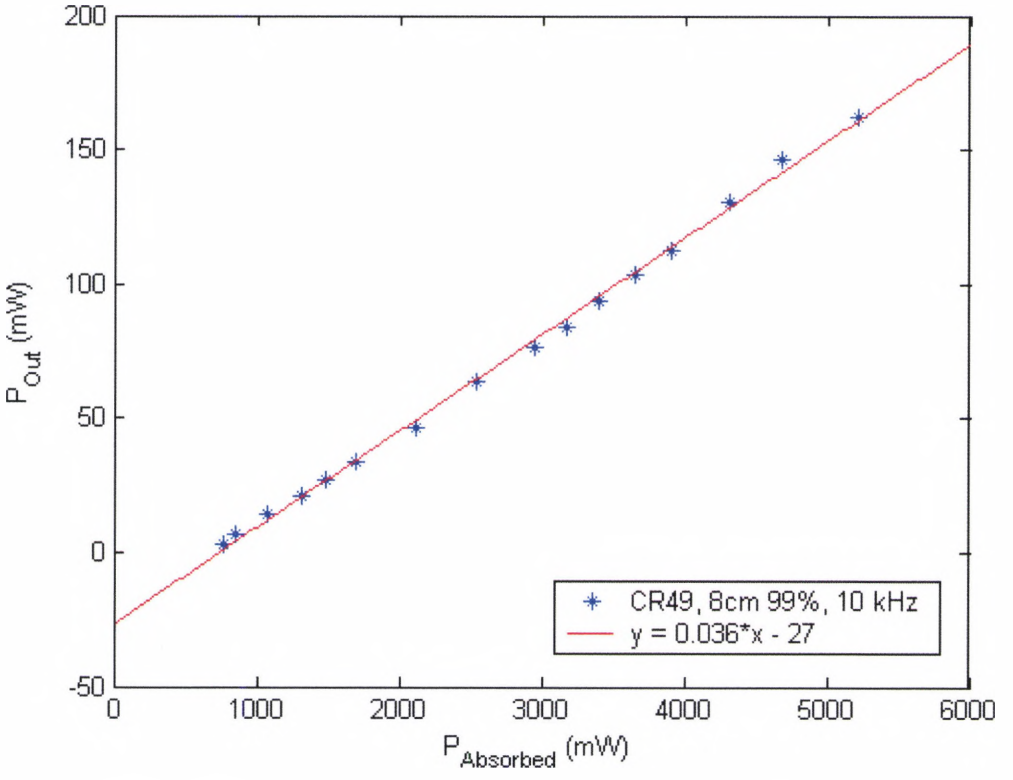

Figure 41: Slope efficiency of CR49, 8cm laser cavity, 10 kHz PRF, 99% outcoupler

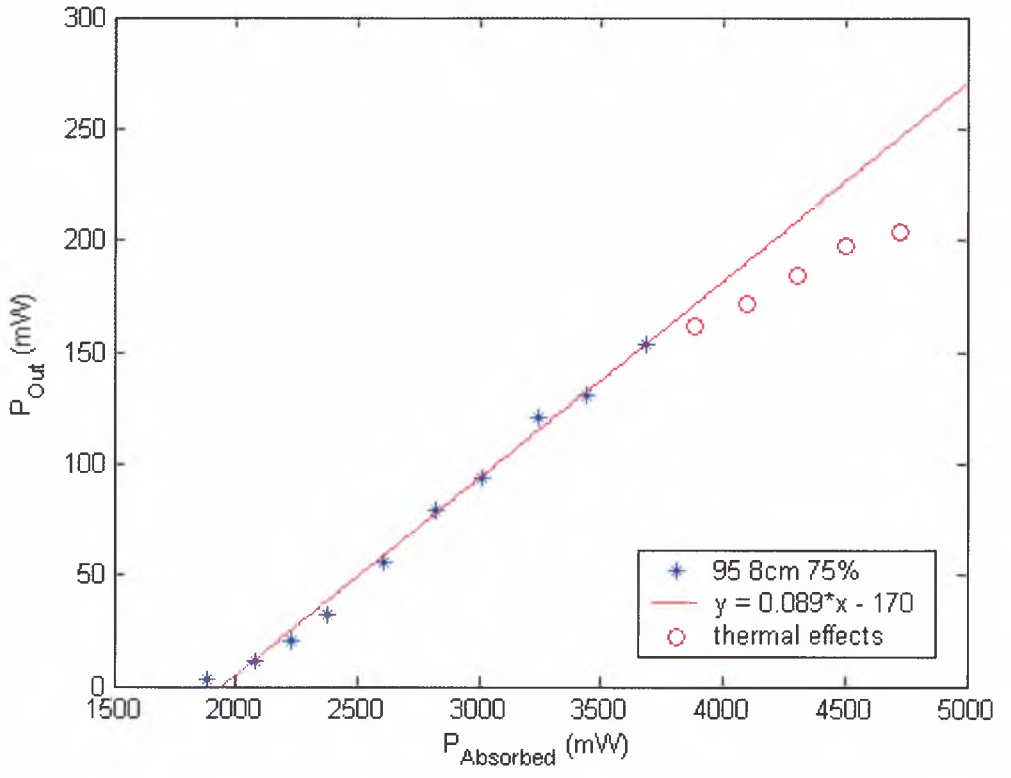

Figure 42: Slope efficiency of CR48, 8cm laser cavity, 10 kHz PRF, 75% outcoupler

In the above experiments, all samples were pumped at a PRF of 10 kHz. In order to maximize the thermal effects, the samples were pumped CW using a thulium fiber laser at input powers up to 8 W. All three of the samples failed to lase under these conditions. Under CW pumping, the threshold was increased to the point where the maximized thermal effects have already destabilized the cavity enough to prevent lasing.

To verify this, CR49 was run with PRF's of 10, 20, 30 and 40 kHz. As the PRF increased, the rest time between pulses decreased, becoming increasingly quasi-CW. In addition, CR48 was run at 10 and 15 kHz as well. CR44 demonstrated thermal lensing at a PRF of 40 kHz (seen in Figure 43) and CR48 showed problems at 15 kHz (seen in Figure 44). Both of these experiments

clearly show the point at which thermal issues become detrimental to the laser cavity performance.

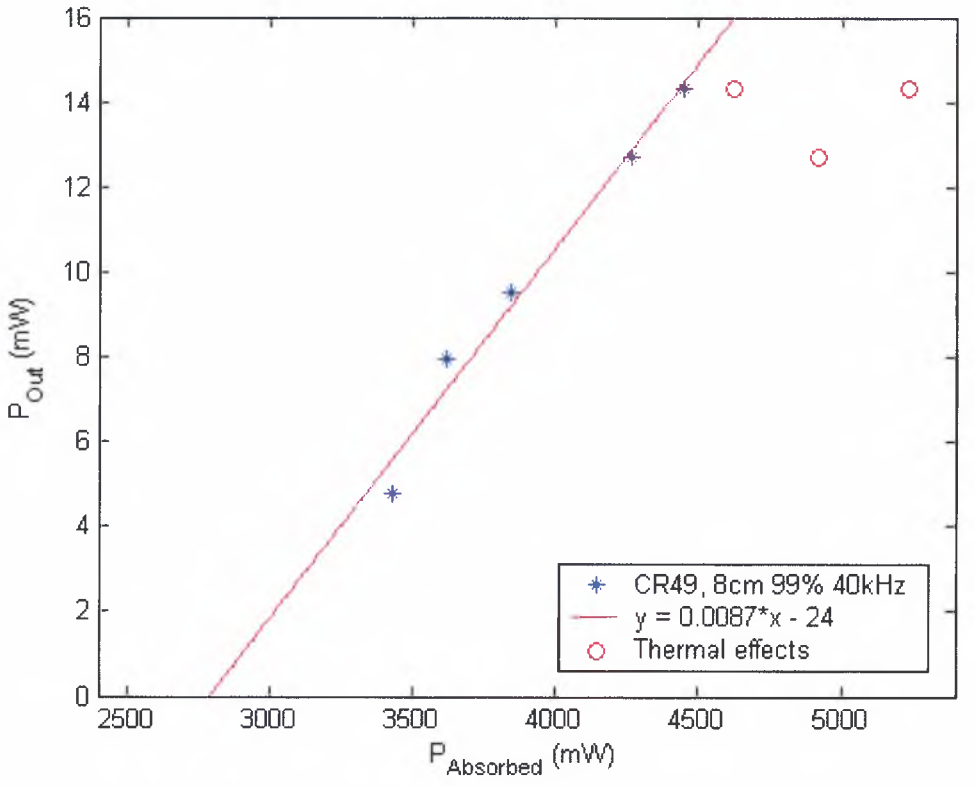

Figure 43: Slope efficiency of CR49, 8cm laser cavity, 40 kHz PRF, 99% outcoupler

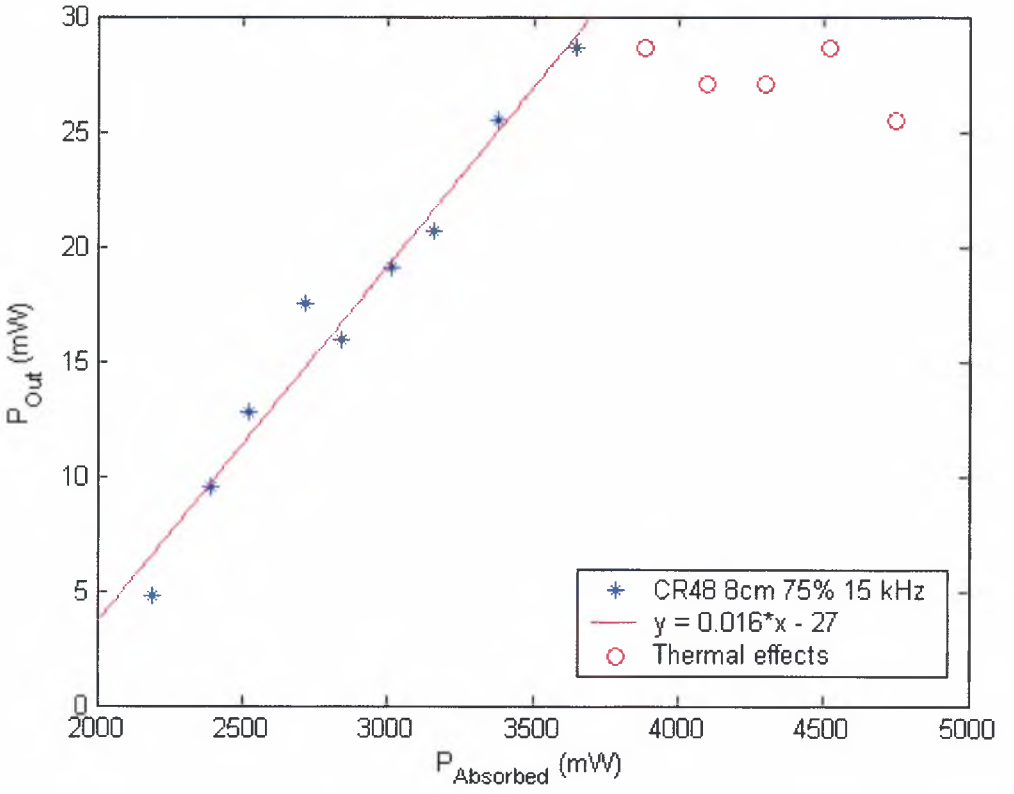

Figure 44: Slope efficiency of CR48, 8cm laser cavity, 15 kHz PRF, 75% outcoupler

A summary of the results for all experiments can be seen below in Table 4. The slope efficiency values marked with an asterisk (*) denote experiments that demonstrated thermal lensing.

Table 4: Summary of results

Sample	Cavity Length (cm)	PRF (kHz)	Outcoupler Transmission (%)	Slope Efficiency(%)
1	8	10	99	9.1
1	10	10	99	7.8
1	14	10	99	5.4
1	18	10	99	2.1
1	8	10	95	15.9
1	8	10	75	23.8
1	8	10	50	18.6
96	8	10	99	3.6
96	8	20	99	2.0
96	8	30	99	1.4
96	8	40	99	0.8*
96	8	10	95	11.0
96	8	10	75	18.8
95	8	10	99	1.7
95	8	10	75	8.9*
95	8	15	75	1.6*

Chapter 8
Conclusion

Thermal lensing in II-VI host compounds will always be a design issue in these types of mid-IR lasers. One way or another, it will have to be addressed. This research has demonstrated an effective design and modeling system that can be used to shorten laser development time and reduce research costs. This research also demonstrated a simple to construct thin disk laser design that has room-temperature operation and is not significantly affected by thermal lensing under pulsed operation. The best average power achieved for this design was 965 mW using CR44 pumped with 4.9 W at 10 kHz PRF with a 75% reflective outcoupler. The maximum power was probably limited by the losses in the cavity due to poor surface mating of the windows as well as scattering Other limiting factors could have included low pump absorption due to single pass pumping as well as increased losses to non-radiative relaxation due to elevated temperature.

Future work in this area could involve improving the modeling to predict time-dependent evolution of thermal lensing as opposed to steady-state solutions. This would be extremely useful in understanding the thermal affects under higher pulse repetition rates and CW pumping. A time-dependent model would allow investigation of how quickly the heat spreads through the sample and how much rest time is need for dissipation of the heat. Further thin disk

designs should be investigated taking into account results obtained in this research. These designs could include multiple disk designs, side-pumped or multiple-angle-pumped designs, use of negative dn/dT materials as compensators, and differential heating/cooling designs to compensate for thermal gradients. The ultimate design would compensate for thermal lensing in real time and allow stable, high-power operation under all conditions.

Appendices

Appendix One: Detailed Model Construction Process

The following instructions are for constructing a 2 mm x 2 mm x 1 mm parallelepiped (referred to as a 'block' by FemLab®) using FemLab® 3.0a, version number 3.0.0.228. The menu commands and dialog boxes are significantly different for other versions. Please consult the FemLab® manual for further information on dialog options and program intricacies.

The first step in constructing a model using FemLab® is to draw the objects. FemLab® has a CAD-type interface for building objects which is accessed through the **Draw** menu. Create the basic shape by choosing **Block** from the **Draw** menu. The configuration dialog seen in Figure 45 can be used to create any size object. Note that all lengths are in meters.

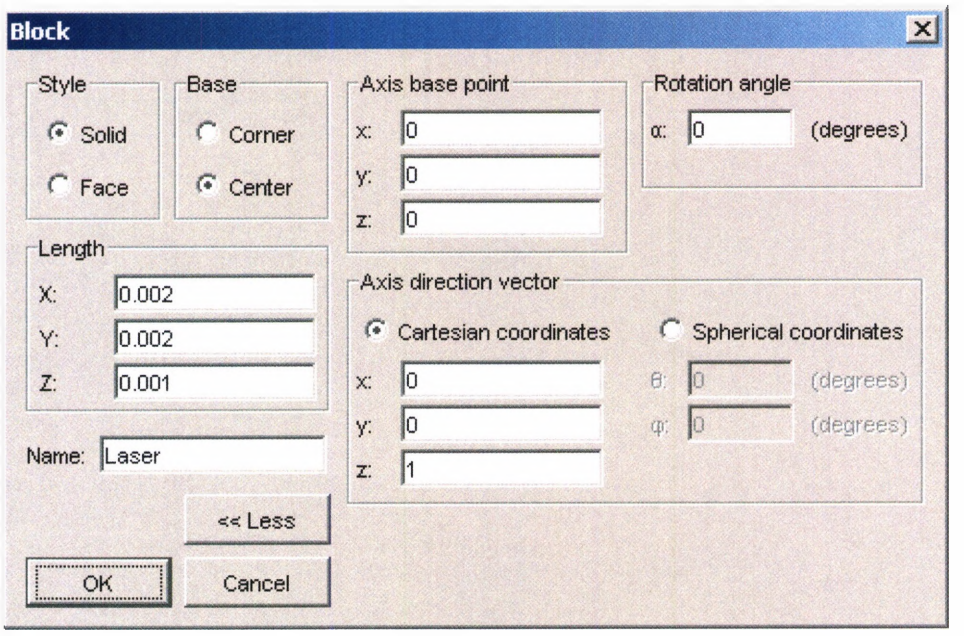

Figure 45: Block-type object configuration dialog

Once the basic geometry of the model is complete, the next step is to set up constants and variables. In the example model the constants needed are the temperature of the heat sinks (T0), the thickness of the laser material (thick), the Gaussian width of the pump beam (sigma) and the power of the pump beam (P). In addition, the integration constants (see section 4.1 Modeling Approach, Assumptions and Limitations) for the Gaussian beams need to be calculated. This setup can be seen in Figure 46.

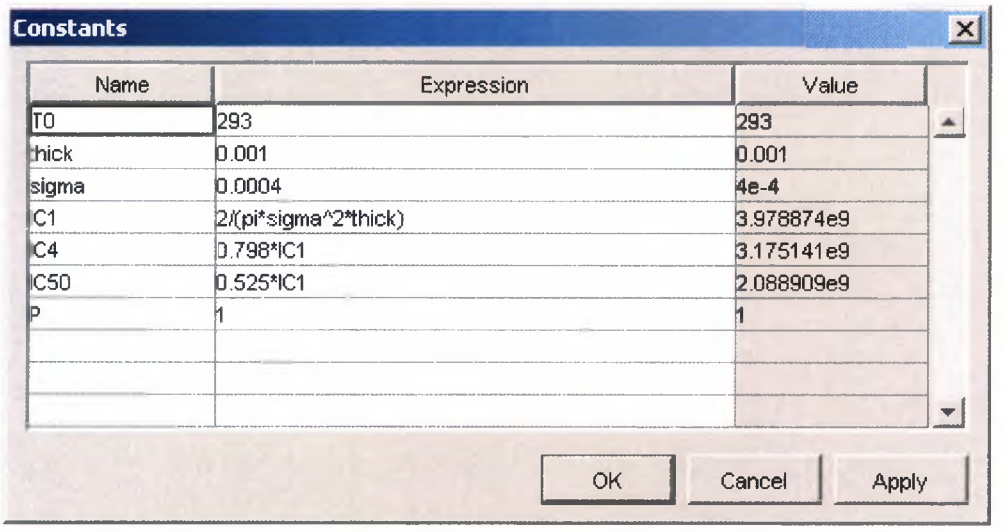

Figure 46: Constants configuration dialog

The next step in the model construction is to define the boundary conditions for the geometry. This is accessed through the **Boundary Settings...** command in the **Physics** menu. In general, there are three types of boundaries in this type of model. Any surface that touches air is considered to be an insulator such that any convective or radiative cooling by air is neglected. The configuration and an example of these types of boundaries can be seen in Figure 47 and Figure 48. Any surface that is to be considered a heat sink or that touches coolant should be set to the value of the heat sink temperature constant (T0). This configuration and an example can be seen in Figure 49 and Figure 50. All other surfaces should be intersections of objects or subdomains and their parameters are solved for by the program (in this example there are none).

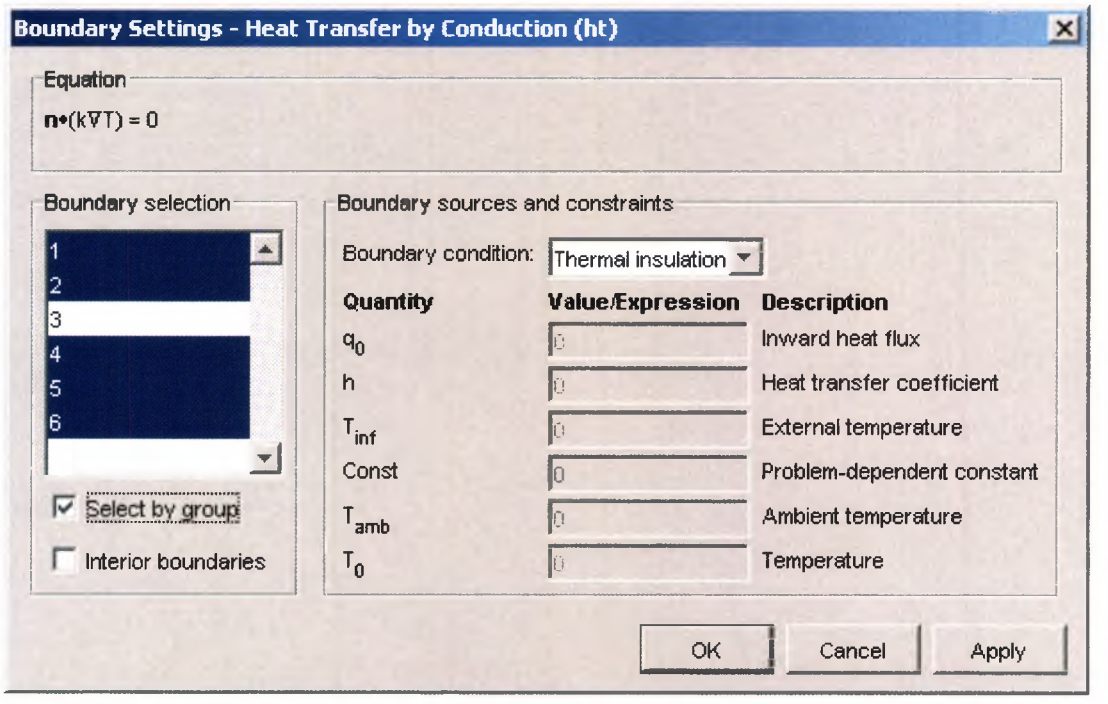

Figure 47: Boundary setting configuration dialog

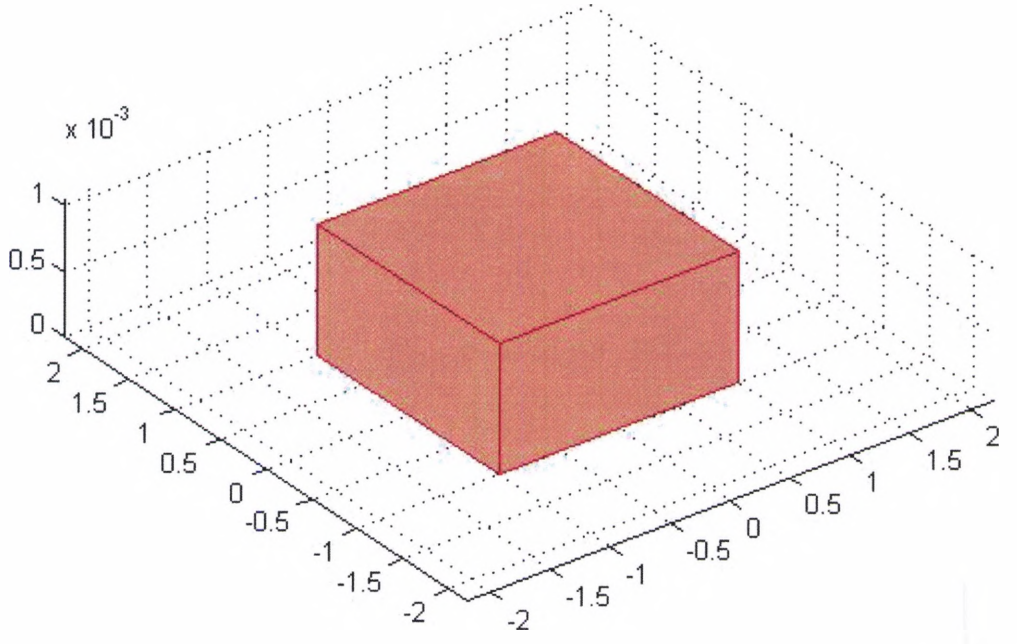

Figure 48: Insulating surfaces example

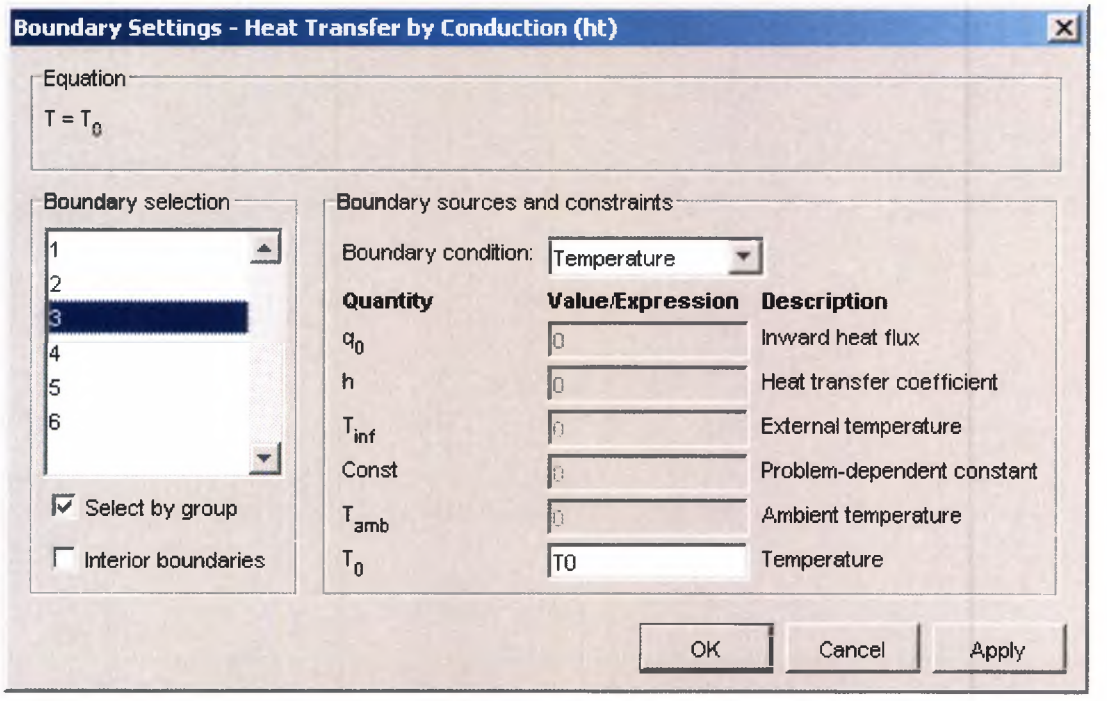

Figure 49: Boundary settings configuration dialog

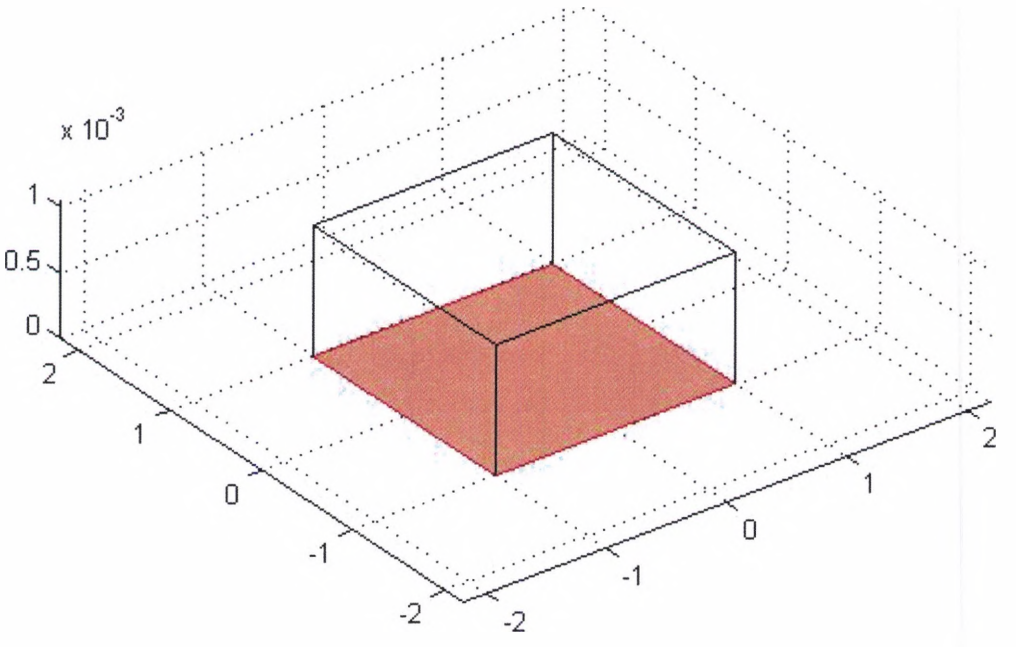

Figure 50: Constant temperature surface example

Once the boundaries have been configured, the configuration of the subdomains can be accessed thorough the **Subdomain Settings...** command in the **Physics** menu. Where the boundary configuration involved geometry surfaces, the subdomain values involve the material properties of the internal volumes of objects. Figure 51 shows the configuration of the main subdomain in our example. Other models may have additional subdomains. Whenever possible, the parameters of the actual material to be used in the experiment should be used in this configuration. Material parameters can be loaded from the supplied materials library or entered in the material library configuration screen, seen in Figure 52, which is accessed through the **Material Library...** command in the **Options** menu. For this model, a defined material, ZnSe was used.

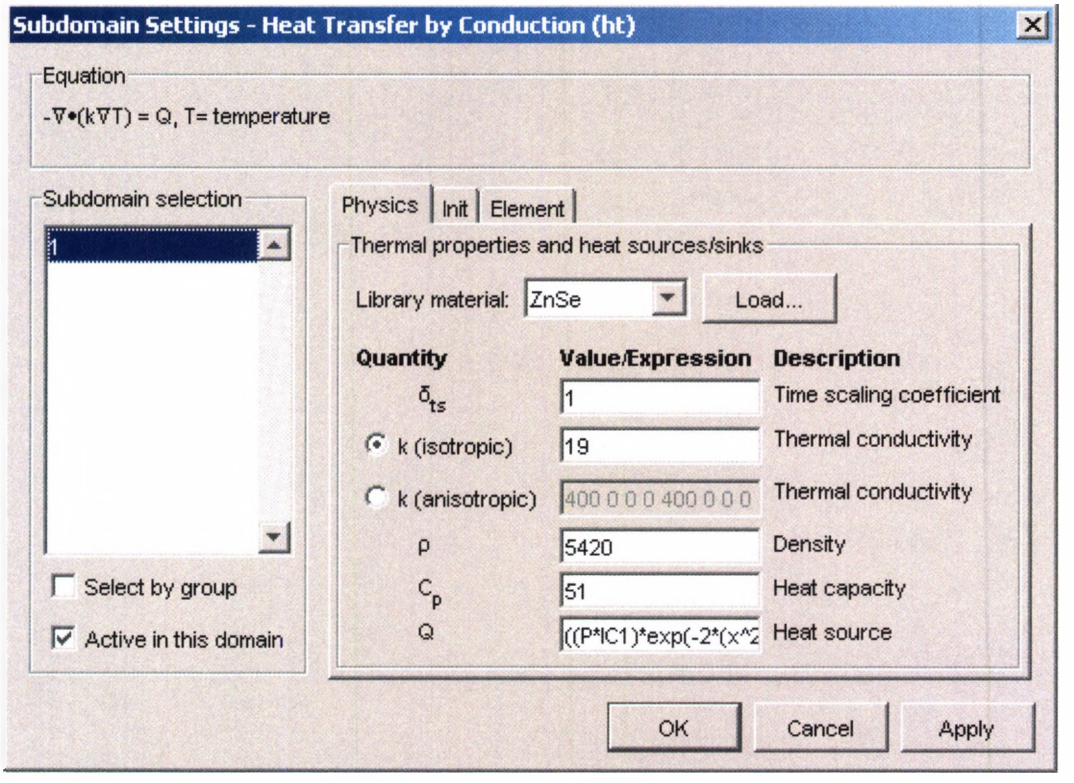

Figure 51: Subdomain settings configuration dialog – coefficients

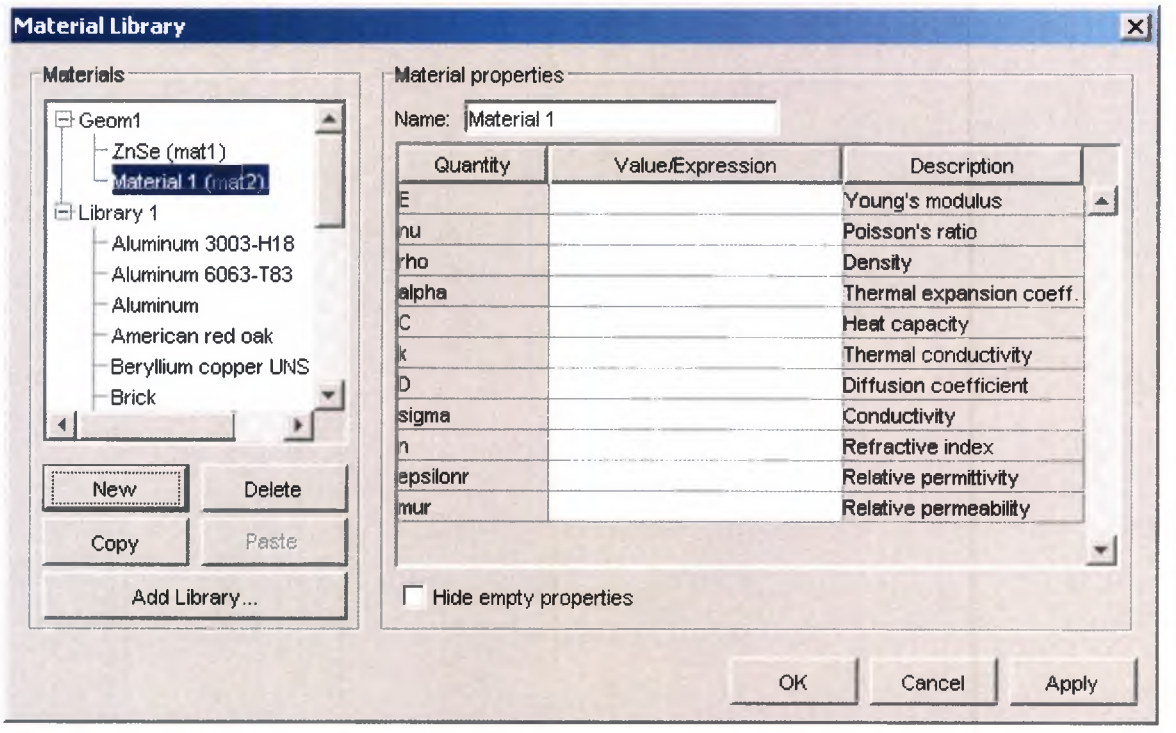

Figure 52: Material library configuration dialog

In addition to defining material parameters, the Q value for any subdomain that is to be absorbing pump power should be set to reflect the Gaussian distribution, including the previously calculated integration constant, as seen in Figure 53.

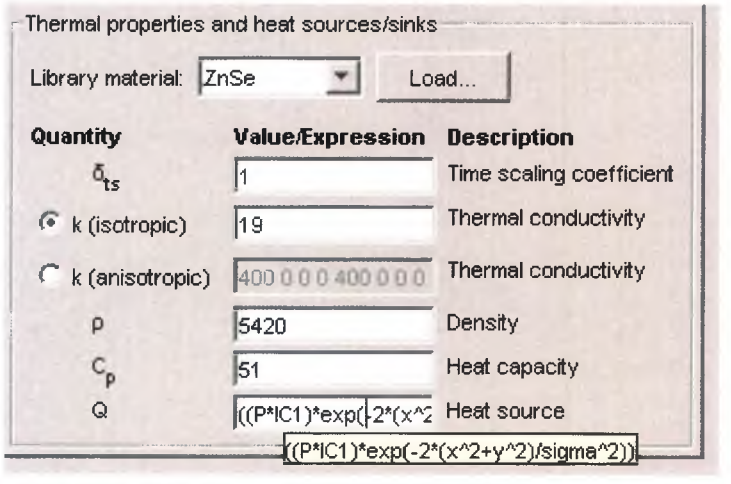

Figure 53: Gaussian power distribution entry

Finally, the initial temperature should be set as in Figure 54 and the settings for the finite element analysis should be set as in Figure 55.

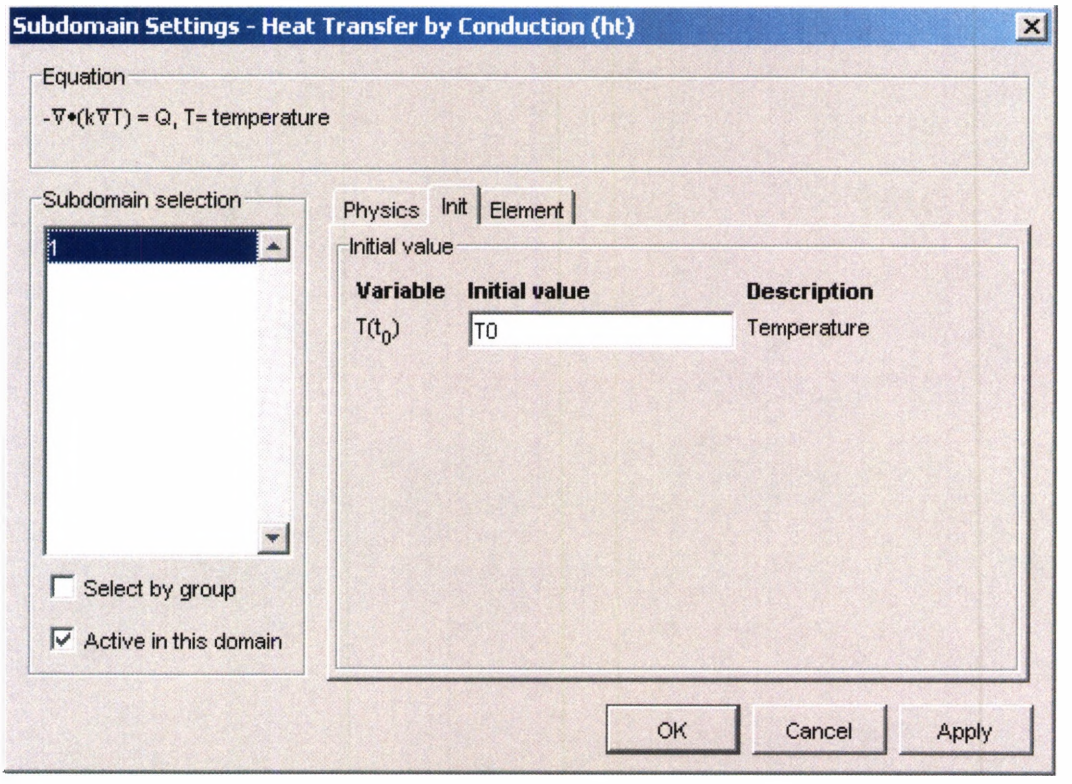

Figure 54: Subdomain settings configuration dialog - initial values

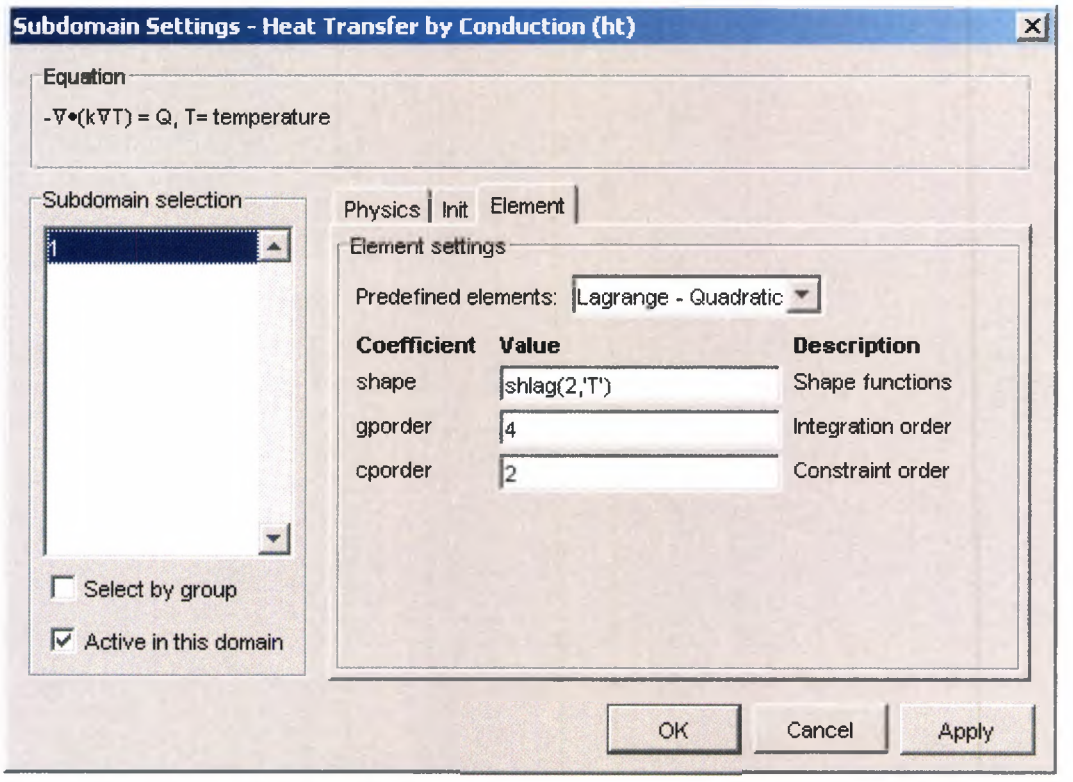

Figure 55: Subdomain settings configuration dialog - finite elements

Appendix Two: MatLab Code

Listing 1: ExponetialFit.m

```
function returnval = ExponetialFit(data,titletext, startoffset, endoffset)

%returnval = ExponetialFit(data,titletext, startoffset, endoffset)
% procedure performs a semi-log plot of data and linear best fit
% returns slope of linear fit ( = lifetime of decay)
% startoffset and endoffset parameters are used to window data for best fit

if nargin < 3
   titletext = 'Exponential Fit'
   startoffset = 0;
   endoffset = 0;
end
x = data(1+startoffset:end-endoffset,1);
y = data(1+startoffset:end-endoffset,2);
logy1 = polyfit(x,log(y),1);
fitline = exp(polyval(logy1,x));
semilogy(x,fitline,'-r',x,y);
title(titletext)
xlabel('Time (sec)');
returnval = 1/logy1(1);
```

Listing 2: thermal_lens.m

```
function f = thermal_lens(fem, nx, ny, nz, n_window);
%**************************************
% FUNCTION thermal_lens(fem, nx, [ny], [nz], n_window)
% function to do line integral along z of temperature and plot 2D result;
%   fem: fem structure exported from FemLab
%   nx: number of points in x data array, usually 51 or 101
%   ny: optional, number of points in y array, defaults to nx
%   nz: optional, number of points in z array, defaults to nx
%   n_window: window size in number of points
%**************************************

if nargin < 2
   nx = 51;
end
if nargin < 3
   ny = nx;
end
if nargin < 4
   nz = nx;
end
if nargin < 5
   n_window = 0;
end
dndt = 70e-6;
xmax = postmax(fem, 'x');
xmin = postmin(fem, 'x');
ymax = postmax(fem, 'y');
ymin = postmin(fem, 'y');
zmax = postmax(fem, 'z')
zmin = postmin(fem, 'z')
% YOU MUST SPECIFY THE Z DIM FOR MODELS WITH WINDOWS AND
RING HEATSINKS
%zmax = 0.002;
%zmin = -0.001;
% find out the baseline temp from the constants
T0 = postmax(fem, 'T0');
% define dimension vectors
xd = linspace(xmin, xmax, nx);
yd = linspace(ymin, ymax, ny);
zd = linspace(zmin, zmax, nz);
% make vectors into a 3D mesh
[x,y,z]=meshgrid(xd, yd, zd);
% get the temperature data from the 'fem' structure for the mesh
Txyz = postinterp(fem,'T',[x(:)';y(:)';z(:)']);
```

```
% replace any NaNs with 293
i = find(isnan(Txyz));
Txyz(i) = T0;
% break the long array into a 3D array
Txyz=reshape(Txyz,size(x));
% find out the length of each section of the array
[dx, dy, dz] = size(Txyz);
% average the temp in the z dir and subtract baseline temp to get
% ave temp rise
T_z_ave = (sum(Txyz,3)/dz) - T0;
% surface plot the average temp rise
xd1 = xd*1000;
yd1 = yd*1000;
figure(1)
surf(xd1, yd1, T_z_ave);
set(gcf, 'Color', 'white');
h = findobj(gcf, 'Type', 'surface');
set(h, 'LineStyle', ':');
axis tight;
zlabel('\DeltaT_{Ave}');
T_x = T_z_ave(:,floor(dx/2)+1); % pulls temperature profile for y=0 in the x
direction
T_x = T_x'; % transposes the matrix to get it in the right orientation
max_ave_temp_rise = max(T_x)
% Focal Length Calculation
% first decide what data window we are fitting to
if n_window > 0
   % if a window is given, create the smaller data sets
   index_start = (nx - 1)/2 - n_window +1;
   index_end = (nx - 1)/2 + n_window + 1;
   x_win = xd(index_start:index_end);
   T_x_win = T_x(index_start:index_end);
else
   % otherwise, take just the middle section of the data and x axis for
   % 20%
   index_start = (nx - 1)/2 - round(nx*.2) +1;
   index_end = (nx - 1)/2 + round(nx*.2) + 1;
   x_win = xd(index_start:index_end);
   T_x_win = T_x(index_start:index_end);
end

% now fit a polynomial to the half-max
poly_constants = polyfit(x_win,T_x_win,2);
% take the first element, the x^2 constant
b = poly_constants(1);
T0Val = poly_constants(3);
```

```
% plot the full data
figure(2)
plot(xd,T_x);
% plot the window data
hold on
plot(x_win,T_x_win,'k-');
plot(x_win,T0Val + b.*x_win.^2,'r:','LineWidth',2);
set(gcf, 'Color', 'white');
axis tight;
ylabel('\DeltaT_{Ave}');
xlabel('Position');
hold off
% calculate the lens power in diopters
f = (4.*(zmax - zmin).*dndt.*b)
disp('diopters');
fl = ['lens power = ', num2str(f), ' m^-1'];
text(0,max_ave_temp_rise/2,fl);
laser_diameter_fit = xd(index_end) - xd(index_start)
```

Listing 3: HSIC.m

```
function IC = HSIC(x1, x2, y1, y2, thick, sigma, order)
%************************************
%   IC = HSIC(x1, x2, y1, y2, thick, sigma, order)
%   Calculates the integration constant needed to
%   normalize the absorbed power density to 1
%************************************

% set up the x and y limits
x = linspace(x1, x2, 101);
y = linspace(y1, y2, 101);
% create a 2D mesh from those co-ords
[x, y] = meshgrid(x, y);
% calculate the heat source for each co-ord in the mesh
H = HSG(x, y, thick, sigma, order);
% integrate the 2D array to get the Absorbed Power Density (volume)
% do not forget to multiply by the thickness to account for
% the integration in the z direction which is considered
% to be uniform for this model
% note that integrations in mat-lab need to be done using the equivalent
% of a Riemann Sum: sum of f(x)*dx
dx = (x2 - x1)/100;
dy = (y2 - y1)/100;
APD = sum(sum(H*dx)*dy)*thick;
IC = 1/APD;
comp = 2/(pi*sigma^2*thick);
ratio = IC/comp;
disp('integration constant = ');
disp(ratio);
disp('*');
disp('2/(pi*sigma^2*zmax)');
```

Listing 4: HSG.m

```
function f = HSG(x,y,zmax,sigma, order)
%**********************************
%   f = HSG(X,Y,ZMAX,SIGMA)
%   HEAT SOURCE GAUSSIAN
%   x = x co-ord
%   y = y co-ord
%   zmax = z thickness
%   sigma = pump beam radius
%**********************************
if nargin < 5
   order = 1;
end
x0 = 0;
y0 = 0;
% normalized
%f = (2/(pi*sigma*sigma*zmax))*exp(-(2*((x - x0).^2 + (y - y0).^2))/(sigma.^2));
% unnormalized
% any order other than 1 needs to be divided by 2
if order > 1
   order = order/2;
end
f = exp(-(2*((x - x0).^2 + (y - y0).^2).^order)/(sigma.^(2*order)));
```

Listing 5: HSICR.m

```
function IC = HSICR(rmax, thick, sigma, order)
%************************************
%   IC = HSICR(r, thick, sigma, order)
%   Calculates the integration constant needed to
%   normalize the absorbed power density to 1
%   for a radial system = round disk
%************************************

% set up the x and y limits
r = linspace(0, rmax, 1001);
% calculate the heat source for each co-ord along the radius
H = HSGR(r, sigma, order);
% integrate to get the Absorbed Power Density (volume)
% do not forget to multiply by the thickness to account for
% the integration in the z direction which is considered
% to be uniform for this model
% and also by 2*pi for the radial symmetry
% note that integrations in mat-lab need to be done using the equivalent
% of a Riemann Sum: sum of f(x)*dx
dr = rmax/1000;
APD = sum(H.*r*dr)*(2*pi)*thick;
IC = 1/APD;
comp = 2/(pi*sigma^2*thick);
ratio = IC/comp;
disp('integration constant = ');
disp(ratio);
disp('*');
disp('2/(pi*sigma^2*zmax)');
```

Listing 6: HSGR.m

```
function f = HSGR(r, sigma, order, r0)
%**********************************
%   f = HSGR(r,SIGMA, ORDER)
%   HEAT SOURCE GAUSSIAN - radial
%   r = radial co-ord
%   sigma = pump beam radius
%   order = gaussian order
%**********************************
if nargin < 3
   order = 1;
end
if nargin < 4
   r0 = 0;
end
% unnormalized
% any order other than 1 needs to be divided by 2
if order > 1
   order = order/2;
end
f = exp(-(2*((r - r0).^2).^order)/(sigma.^(2*order)));
```

References

[1] L. D. DeLoach, R. H. Page, G. D. Wilke, S. A. Payne, and W. F. Krupke, "Transition metal-doped zinc chalcogenides: spectroscopy and laser demonstration of a new class of gain media," IEEE J. Quantum Electronics **32**(6), 885-895 (1996).

[2] U. Hömmerich, X. Wu, and V. R. Davis, "Demonstration of room-temperature laser action of 2.5 μm from Cr^{2+}:$Cd_{0.85}Mn_{0.15}Te$," Optics Letters **22**(15), 1180-1182 (1997).

[3] J. B. McKay, K. L. Schepler, and G. C. Catella, "Efficient grating tuned mid-IR Cr^{2+}:CdSe laser," Optics Letters **24**(22), 1575-1577 (1999).

[4] R.H. Page, K. I. Schaffers, L.D. DeLoach, G.D. Wilke, F.D. Patel, J.B. Tassano, S. A. Payne, W.F. Krupke, K-T. Chen, and A. Burger, "Cr^{2+}-doped zinc chalcogenides as efficient, widely tunable mid-infrared lasers," IEEE J. Quantum Electronics **33**(4), 609-619 (1997).

[5] K.L. Schepler, R.D. Peterson, P. A. Berry, and J. B. McKay, "Thermal Effects in Cr^{2+}:ZnSe Thin Disk Lasers," J. Quantum Electronics (to be published).

[6] J. A. Harrington, "A review of transmitting, hollow waveguides", Fiber and Integrated Optics **19**, pp.211-217 (2000).

[7] L. B. Shaw, et al, "Mid-wave IR and long-wave IR laser potential of rare-earth doped chalcogenide glass fiber", IEEE J. Quantum Electronics **48**(9), pp.1127-1137 (2001).

[8] J. B. McKay, "Background Research," in *Power scaling feasibility of chromium-doped II-VI laser sources and the demonstration of a chromium-doped zinc selenide face-cooled disk laser*, Dissertation (Air Force Institute of Technology, 2003) pp. 29-31.

[9] W. Koechner, *Solid State Laser Engineering, 3rd Edition* (New York: Springer-Verlag, 1992), pp. 432–433.

[10] C. Stewen, M. Larionov, and A. Giesen, "Yb:YAG thin disk laser with 1 kW output power," in *OSA Trends in Optics and Photonics, Advanced Solid State Lasers*, H. Injeyan, U. Keller, and C. Marshall, ed. (Optical Society of America, Washington, DC., 2000) pp. 35-41.

[11] J. B. McKay, W. B. Roh, and K. L. Schepler, "4.2 W Cr2+:ZnSe face cooled disk laser," in *OSA Trends in Optics and Photonics, Conference on Lasers and Electro-Optics*, (Optical Society of America, Washington DC 2002) pp. 119-120.

[12] S. Erhard, M. Karszewski, C. Stewen, A. Giesen, K. Contag, and A. Voss, "Pumping schemes for multi-kW thin disk lasers," in *OSA Trends in Optics and Photonics, Advanced Solid State Lasers*, H. Injeyan, U. Keller, and C. Marshall, ed. (Optical Society of America. Washington, DC., 2000).

[13] J. B. McKay, "Material Characterization," in *Power scaling feasibility of chromium-doped II-VI laser sources and the demonstration of a chromium-doped zinc selenide face-cooled disk laser*, Dissertation (Air Force Institute of Technology, 2003) pp. 1-3.

[14] R.H. Page, L.D. DeLoach, K. I. Schaffers, F.D. Patel, R. J. Beach, S. A. Payne, W.F. Krupke, "Recent developments in Cr^{2+}-doped II-VI compound lasers," in *OSA Trends in Optics and Photonics, Advanced Solid State Lasers*, S. Payne, and C. Pollack, ed. (Optical Society of America, Washington, DC., 1996) pp. 130-136.

[15] D. Findlay and R. A. Clay, "The measurement of internal losses in 4-level lasers", Physics Letters **20**(3), 277-278 (1966).

[16] M. Weber, *Handbook of Laser Science and Technology, Vol. IV, Optical Materials, Pt. 2,* (Chemical Rubber Company Press, Florida, 1986).

[17] W. Koechner, *Solid State Laser Engineering, 3rd Edition* (New York: Springer-Verlag, 1992), p. 391.